



BUNDESREPUBLIK
DEUTSCHLAND

Bundesanstalt für
Geowissenschaften
und Rohstoffe (BGR)

Hannover

PEOPLE'S REPUBLIC
OF BANGLADESH

Geological Survey
of Bangladesh (GSB)

Dhaka

Geo-Information for Urban Planning and Adaptation to Climate Change (GPAC)

Remote Sensing Information for Urban Planning of Kushtia Town and Surroundings

Lukas Wimmer

Nicolas Wagener

Remote Sensing Working Group BGR

Hannover, February 2021

Remote Sensing Information for Urban Planning of Kushtia Town and Surroundings

Authors: Lukas Wimmer (BGR), Chapter 2
Nicolas Wagener (BGR), Chapter 1

Project Number: 2016.2062.4

BGR Number: 05-2394

Project Partner: Geological Survey of Bangladesh (GSB)

Pages: 69

Place and date of issuance: Hannover, February 2021

To be cited as:

Wimmer, L. and Wagener, N. (2021): Remote Sensing Information for Urban Planning of Kushtia Town and Surroundings, BGR Project Number: 05-2394.

Table of Contents

List of Figures.....	I
List of Tables.....	III
List of Abbreviations.....	IV
1 Introduction to Remote Sensing	1
1.1 Fundamentals of Optical Remote Sensing.....	2
1.2 Fundamentals of RADAR Remote Sensing	3
2 Products.....	5
2.1 Land-use Map.....	5
2.2 River Shifting Change Detection Map.....	14
2.3 Inundation Map.....	25
References.....	30
Annexure A: Maps.....	i
Annexure B: Google Earth Engine Code	xxi
Annexure C: Data	xxv

List of Figures

- Figure 1:** Passive and active sensors (Source: BGR). 2
- Figure 2:** Filling of agricultural land with river sand in Faridpur. Photo: L. Wimmer, 11/2019. 5
- Figure 3:** Workflows of the Land-use classification. 8
- Figure 4:** Mean signatures of the merged training areas.....10
- Figure 5:** Workflows of the River Shifting Change Detection analysis.16
- Figure 6:** Reflectance of water, soil and vegetation at different wavelengths; the wavelength areas used by the NDWI are highlighted in green (green bands) and red (NIR bands), modified after SEOS-PROJECT.EU, 2020.18
- Figure 7:** Workflow of the Google Earth Engine processing of the inundation mapping method.28

Annexure A

- Figure A1:** Sentinel-2 Dataset of the Kushtia Region, 22.09.2019 (RGB 4-3-2).i
- Figure A2:** Land use in September 2019 in Kushtia region based on Sentinel-2 data..... ii
- Figure A3:** Land use in September 2019 in Kushtia project area based on Sentinel-2..... iii
- Figure A4:** Status of Urban Development in Sep. 2019 in Kushtia project area. iv
- Figure A5:** Masked Sentinel-2 Dataset of the Kushtia Region, September 2019 (RGB 4-3-2).v
- Figure A6:** Overview of the region around Kushtia (Landsat TM, RGB 321, 06.02.2010). vi
- Figure A7:** Normalized Difference Water Index (NDWI), based on Sentinel-2 imagery (24.02.2019). vii
- Figure A8:** Normalized Difference Water Index (NDWI), based on Sentinel-2 imagery (24.02.2019), Threshold of -0.15. viii
- Figure A9:** Location of the Padma River System based on NDWI from 1973..... ix
- Figure A10:** Location of the Padma River System based on NDWI from 1980..... x
- Figure A11:** Location of the Padma River System based on NDWI from 1990..... xi
- Figure A12:** Location of the Padma River System based on NDWI from 2000..... xii
- Figure A13:** Location of the Padma River System based on NDWI from 2010..... xiii
- Figure A14:** Location of the Padma River System based on NDWI from 2019..... xiv
- Figure A15:** Location of the Padma River System based on NDWI from 2010..... xv
- Figure A16:** Change Detection of Padma River System of February 1973, 2000 and 2019.xvi
- Figure A17:** Active and Passive Areas of the Padma River System in Kushtia, based on Satellite Data of 1973, 1980, 1990, 2000, 2010 and 2019. xvii

Figure A18: Inundation in June/July 2015-2020 in Kushita study area.....xviii
Figure A19: Mean Sentinel-1 image of June/July 2020 in Kushtia study area..... xix
Figure A20: Inundation in June/July 2020 in Kushita study area..... xx

List of Tables

Table 1: Overview of the Copernicus Sentinel-2 satellite image used for the classification. Blue color represents the spectral band subset used in the analysis. 7

Table 2: Overview of the number of training areas per class.....10

Table 3: Accuracy Assessment, Sentinel-2 dataset (22.09.2019).....12

Table 4: Overview of the satellite images and their bands used for the analysis (EUROPEAN SPACE AGENCY 2017; UNITED STATES GEOLOGICAL SURVEY n.d.).....15

Table 5: Overview of the parameters and setting changes for the atmospheric correction of Sentinel-2 data.17

Table 6: Thresholds to discriminate between river system and other values.19

Table 7: Overview of the characteristic values per year.20

Table 8: Legend of the raster values in the change detection map.....20

Table 9: Overview of the characteristic values per year for the mapping of active/passive river system areas.21

Table 10: Legend of the raster cell values in the map of active/passive river system areas. 21

List of Abbreviations

BWDB	Bangladesh Water Development Board
dB	Decibel (unit)
DOS	Dark Object Subtraction
ESA	European Space Agency
GSB	Geological Survey of Bangladesh
InSAR	Interferometric Synthetic Aperture Radar
Landsat MSS	Landsat Multispectral Scanner System
Landsat OLI	Landsat Operational Land Imager
Landsat TM	Landsat Thematic Mapper
LEDAPS	Landsat Ecosystem Disturbance Adaptive Processing System
NASA	National Aeronautics and Space Administration
NIR	Near Infrared
NDWI	Normalized Difference Water Index
PSI	Persistent Scatterer Interferometry
RADAR	Radio Detection and Ranging
SAR	Synthetic Aperture Radar
SWIR	Shortwave Infrared
TIR	Thermal Infrared
UAV	Unmanned aerial vehicle
USGS	United States Geological Survey

1 Introduction to Remote Sensing

Remote sensing has been variously defined, but basically is the science that describes the collection of physical information, interpretation and extraction of information acquired over an object or area of interest without having physical contact, by the use of remote sensing instruments. The term information refers to a wide range of observable quantities, such as reflected solar radiation across the electromagnetic spectrum and emitted thermal radiation measured from handheld, unmanned aerial vehicle (UAV), airborne or spaceborne imaging sensors and received back-scattered microwave radiation equipment. Availability and effective exploitation of such data has facilitated advances in many applied fields (CHAMBELL, 1996; USTIN, 2004)

The availability and capacity of remote sensing data is comprehensive and huge, therefore the application of remote sensing data to identify and monitor land surfaces and environmental conditions has expanded enormously and remotely sensed data are an essential tool in natural resource management. Climatic changes, desertification processes, forest fires, glaciers melting, water pollution, land cover and vegetation status can be observed thanks to remote sensors onboard of aircraft or satellites orbiting around the earth. Remote sensors onboard of aircraft and satellites allow for a synoptic view of the earth surface at different wavelengths of the electromagnetic radiation at the same time (multi-spectral, -frequency), with (high-) frequent time interval and scale (multi-resolution).

Sensors can be divided into two groups: Passive sensors depend on an external source of energy, usually the sun. Sun radiation is reflected and emitted from the earth surface and collected by a wide variety of optical sensors. Active sensors have their own source of energy. These sensors send out a signal and measure the amount reflected back, and do not depend upon varying illumination conditions (PRASAD ET AL., 2011) (see Fig. 1).

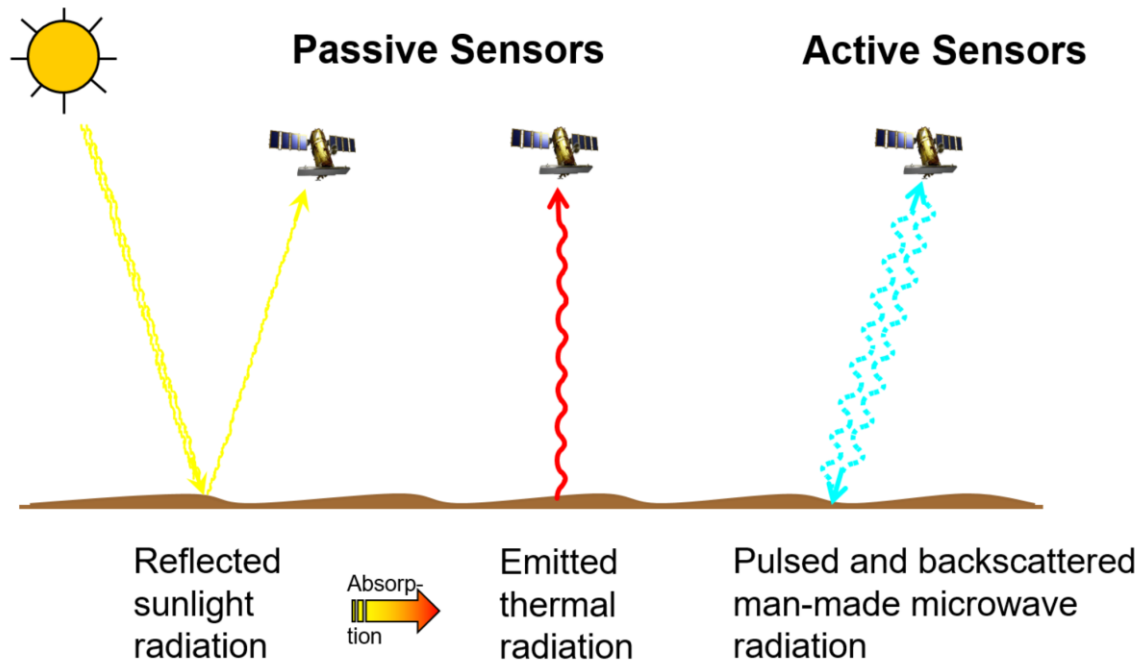


Figure 1: Passive and active sensors (Source: BGR).

1.1 Fundamentals of Optical Remote Sensing

Optical remote sensing involves acquisition and analysis of optical data, based on solar illumination and the detection of electromagnetic radiation reflected from targets on the ground. Optical Remote Sensing deals with those part of electromagnetic spectrum characterized by the wavelengths from the visible (from 0.4 μm) to the near infrared (NIR) and short wave infrared (SWIR) up to thermal infrared (TIR, 15 μm), collecting radiation reflected and emitted from the observed surfaces (see Fig. 1).

Optical remote sensing is a passive technique for earth observation, which is exposed to a strong interaction of the electromagnetic radiation within the atmosphere at its operating frequencies and to the presence of clouds. Both factors constitute important limitations on the potential observation of the earth’s surface.

Analysis is based on the spectral differences of materials, as materials reflect and absorb differently at different wavelengths, resulting in a specific and unique “spectral footprint”. Thus, the targets can be differentiated by their spectral reflectance signatures in the remotely sensed images (SABINS, 1996; RENCZ, 1999).

Optical remote sensing systems are classified depending mainly on the number of spectral bands used in the imaging process. Advances in imaging hardware enabled availability of high spatial, spectral and temporal resolution (PRASAD ET AL., 2011).

A wide range of applications is still based on multispectral imaging systems e.g. Sentinel-2, Landsat-OLI, even so hyperspectral sensors show rapid development on all platforms from UAV to spaceborne carriers.

1.2 Fundamentals of RADAR Remote Sensing

RADAR is an acronym for *RA*dio *DE*tectio*N* *AN*d *R*ang*ING* and describes an object-detection and active imaging system using radio waves (see Fig. 1). The electromagnetic waves used for imaging radars have wavelengths in the order of several centimeters up to roughly one meter. Since earth's atmosphere has a high penetrability in this part of the electromagnetic spectrum, radar-imaging systems are highly independent from weather conditions in the atmosphere.

The accuracy of an imaging radar is defined by two measures: the resolution along the line-of-sight (range resolution) and the resolution along the flight path of the carrier platform (azimuth resolution). The azimuth resolution depends on the antenna aperture: the larger the distance to the area of interest, the larger the antenna must be. For space-borne missions this leads to unrealistic demands on the size of the antenna mounted on the satellite (WOODHOUSE, 2006). To overcome this obstacle, Synthetic Aperture Radar (SAR) exploits the Doppler Effect to synthesize a larger virtual antenna through the combination of several return signals (echoes).

The signal received at the sensor has a frequency variation induced as a result of the platform motion. This effect is known as Doppler shift, a well-known phenomenon in physics. Since the resolution depends on the time, a particular object on the ground is illuminated by the radar beam, making use of the Doppler shift to combine several backscattered echoes effectively results in increasing the duration of irradiation. As this is in effect equal to increasing the antenna aperture size of which the illumination time is a direct function, the term Synthetic Aperture Radar (SAR) is used to describe such an imaging system (RICHARDS, 2009).

SAR sensors are usually mounted on an airborne or space-borne platform and have a side-looking imaging geometry. While the carrier platform moves forward, the SAR system continuously emits and receives electromagnetic pulses. The emitted radiation interacts with objects on the surface that will then backscatter a portion of the signal to the sensor. How big that portion will be, depends on the physical and electrical properties of the objects (FORNANO & PASCAZIO, 2014). At the sensor, both amplitude and phase of the backscattered signal are received (MOREIRA ET AL., 2013). While the

amplitude is related to the object properties (material, roughness, dielectric properties, etc.), the phase is a function of the sensor-target distance.

Synthetic aperture radar (SAR) remote sensing is used today in a wide range of applications and offers a number of complementary and additional capabilities with regard to optical remote sensing. For instance, it can be used to acquire images at night and almost weather independent, to determine soil moisture, biomass or to measure terrain deformations. The ranging capabilities of SAR are used in various ways. Radar interferometry (InSAR) is one such application and allows the estimation of ground deformation and / or topography from (at least) two SAR acquisitions making use of the phase information contained in both images. Multi-temporal InSAR approaches such as Persistent Scatterer Interferometry (PSI) allow the precise estimation (with millimeter accuracy) of surface deformation for specific point targets over long time periods.

2 Products

2.1 Land-use Map

The fast growing population and the trend to move to urban areas leads to a dynamic change in land use. New urban areas are developed by filling agricultural land with river sand to make the building ground more resilient to flooding (see Fig. 2).

The overall goal of this analysis is the comprehensive mapping of the 2019 land-use in Kushtia to derive information on existing and newly established filled areas. The resulting maps will be used in further analyses together with a geomorphological map as a basis for the regionalization of drilling points. Freely available optical satellite data and a supervised classification method allow for the mapping of the land-use.



Figure 2: Filling of agricultural land with river sand in Faridpur. Photo: L. Wimmer, 11/2019.

Land-use maps using the classes “Water”, “Bare Soil”, “Urban”, “Rural Settlements” and “Agriculture” are provided for September 2019. An overview map shows the land-use of the study area as well as the surrounding rural areas (Fig. A2). A map, focusing on the study area presents the land-use within the city of Kushtia (Fig. A3).

The main focus of this analysis is the distribution of filled and non-filled areas from the land-use map by reclassification of the five above-mentioned classes. A third map presents these areas within the study area of Kushtia (Fig. A4).

To process the land-use maps, a supervised classification method based on interactively selected training areas is used. These areas are interactively chosen from the original satellite image and represent the spectral properties of a certain land-use class. The supervised classification classifies the satellite image by comparing all the image values with the selected training areas.

Data

The land use classification is based on a cloud-free image from the Copernicus Sentinel-2 mission for the period of the Bangladesh dry season between October and April and the transition times before and after it. To be able to receive results on the most recent land-use and in order to map water areas comprehensively, a satellite image from the early dry season 2019/2020 is required. Different atmospheric conditions during the sensing times of the images can result in different image features of the same ground objects. Therefore, atmospheric corrected images are mandatory, to allow comparison with future land use maps based on Sentinel-2 data. An atmospheric correction eliminates the atmospheric effects in an image and results in a surface reflectance image that characterizes the spectral surface properties. The atmospherically corrected image, showing the overview area cloud-free, from the 22. September 2019 is used for further processing (see Annexure C: Data).

As input for the land use mapping, all bands with the resolution of 10m and 20m of the image are used (Tab. 1). This selection enables the classification method to accurately characterize the land-use classes by using all available spectral properties of the ground objects.

Table 1: Overview of the Copernicus Sentinel-2 satellite image used for the classification. Blue color represents the spectral band subset used in the analysis.

Sensing Date	Bands		Wavelengths	Spatial Resolution
22.09.2019	1	Coastal Aerosol	417nm – 471nm	60m
	2	Blue	399nm – 595nm	10m
	3	Green	515nm – 605 nm	10m
	4	Red	627nm – 703nm	10m
	5	Near Infrared	685nm – 723nm	20m
	6		722nm – 758nm	20m
	7		754nm – 810nm	20m
	8		690nm – 980nm	20m
	8A		832nm – 898nm	20m
	9	Water Vapor	919nm – 971nm	60m
	10	Cirrus	1299nm – 1449nm	60m
	11	Shortwave Infrared	1471nm – 1757nm	20m
12	1960nm – 2444nm		20m	

Methods

The workflow of the classification is visualized in Fig. 3.

Preprocessing

To prepare the image for the classification, a spatial subset and a spectral subset are created. The spatial subset shows an overview of the study area of Kushtia as well as the surrounding rural areas (Fig. A1). The spectral subset includes the above-mentioned (Tab. 1) Sentinel-2 bands (Band 2, 3, 4, 5, 6, 7, 8, 8A, 11, 12). Subsequent, all image bands with 20m resolution are resampled to a 10m spatial resolution to keep the information of the higher resolution 10m bands.

At two locations, the image is showing smoke (Fig. A1). To avoid misclassifications, these areas are masked from the satellite image for further processing (Fig. A5).

Classes and Training Areas

The purpose of the land-use classification is to derive information on urban settlement structures. Accordingly, the two classes "Urban" and "Rural Settlements" are used for the description of these structures. "Agriculture" and "Bare Soil" are chosen to describe the undeveloped areas in general. Water areas are represented by the class "Water".

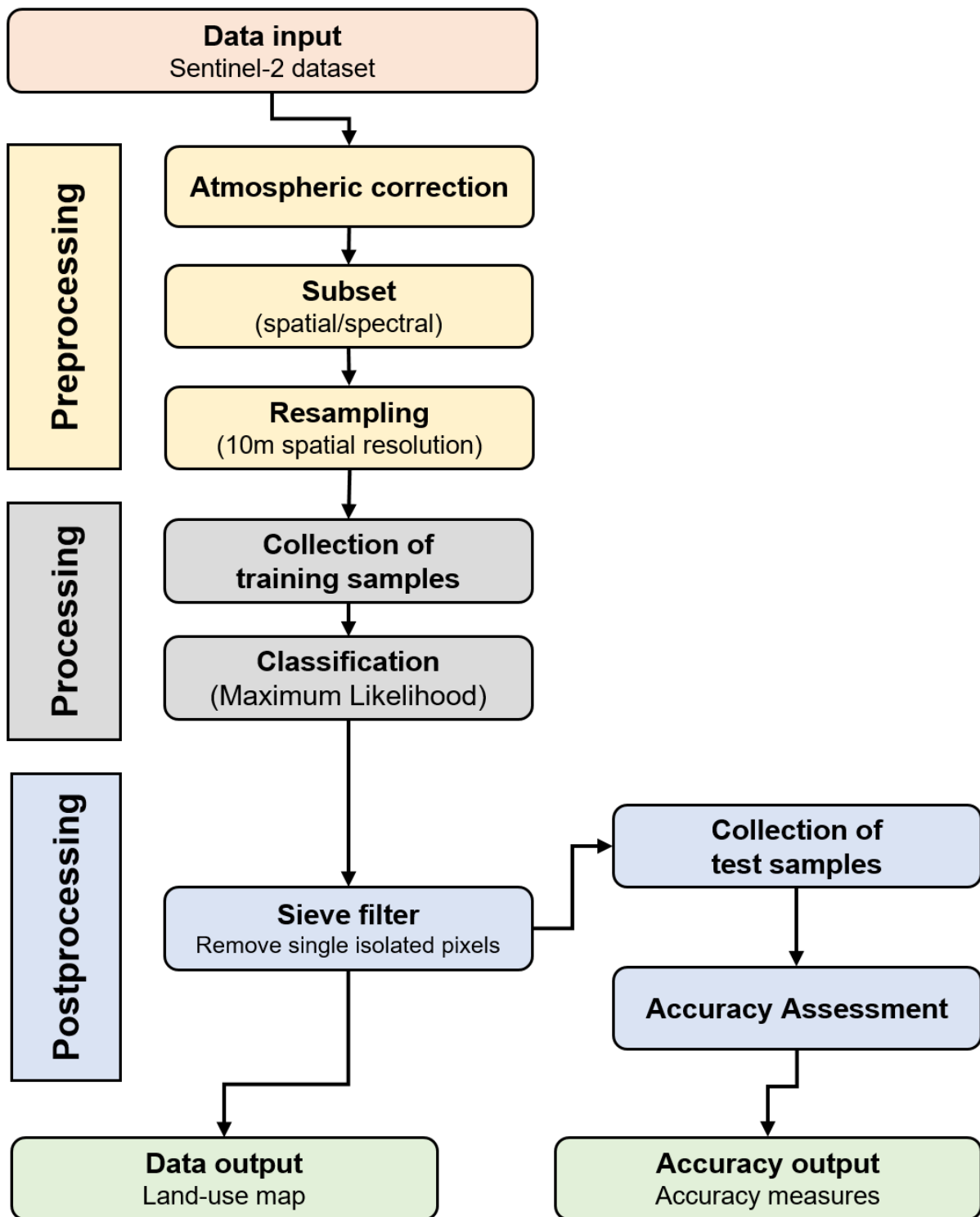


Figure 3: Workflows of the Land-use classification.

These classes are based on the CORINE Landcover (CLC) program (EUROPEAN ENVIRONMENT AGENCY, 2019). CORINE Landcover is a program of the European Commission to standardize the most important forms of land cover for environmental policy development. The standardized classes are based on biophysical characteristics of the Earth's surface (EUROPEAN ENVIRONMENT AGENCY, 2017).

"Water" includes all open water bodies, such as river, canals, channels, lakes and ponds. "Bare Soil" includes all surfaces of bright bare soil, such as riverbanks, pointbars and filled areas for urban development. "Urban" includes residential and industrial buildings without tree cover. Furthermore, it includes streets, railway lines and sealed surfaces. "Rural Settlements" include the city suburbs and rural villages that have tree coverage. "Agriculture" are all areas of farmland, such as cropland (rice, vegetables, etc.) or pasture land (for cattle, goats, etc.).

Training areas for all classes are selected from the Sentinel-2 dataset (see Tab. 2). To receive an acceptable classification result, the training areas must be both representative and complete for their land-use classes (LILLESAND ET AL., 2015).

All land-use classes have non-uniform spectral characteristics in common. For example, in the "Urban" class, the spectral characteristics of tin shacks and high-rise buildings differ. The "Agriculture" class includes spectral characteristics of different crops and in the "Water" class, different water qualities also differ spectrally. Different soil types in the "Bare Soil" class also have different spectral characteristics. The "Rural Settlements" class contains areas with different tree species, which result in different spectral characteristics.

The training areas of the land-use classes are required to represent these different spectral characteristics. The number of training areas therefore depends on the spectral variability within a land-use class (see Tab. 2).

The training areas are dispersed throughout the Sentinel-2 dataset to increase the representation of all variations in the land-use classes (LILLESAND ET AL., 2015).

Table 2: Overview of the number of training areas per class.

Class	Number of Training Areas
Agriculture	25
Bare Soil	15
Rural Settlements	10
Urban	15
Water	20

To show the spectral variabilities of the individual classes, the spectral profiles of the classes are shown in Fig. 4. Each curve represents the averaged spectral signatures of all training areas per class, based on the Sentinel-2 data set of 22.09.2019. Fig. 4 shows the spectral separability of the classes over the whole band range (see Tab. 1).

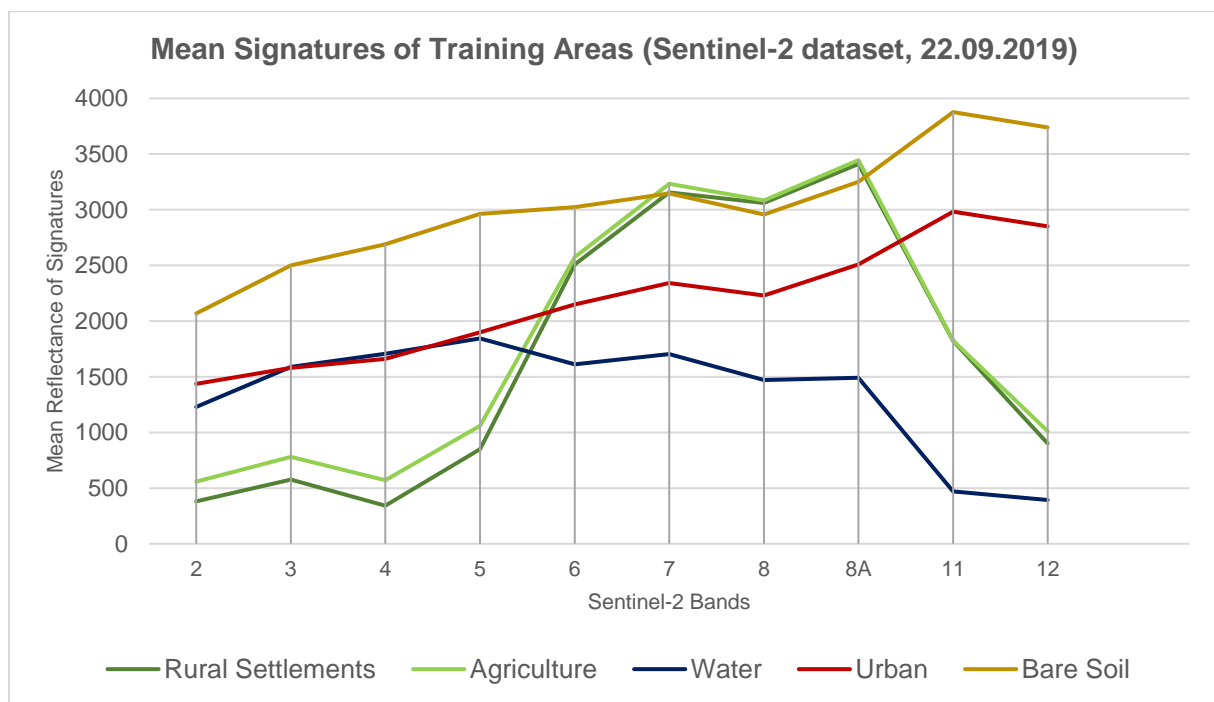


Figure 4: Mean signatures of the merged training areas.

The spectral curves of the classes “Agriculture” and “Rural Settlements” have similar spectral signatures. The reason for these similarities is that the class “Rural Settlements” is dominated by tree coverage and therefore represents a strong vegetation signal. Both classes show vegetation-typical characteristics, such as the “red edge” (a significant increase of reflection in the near infrared bands 5 and 6

compared to the visible bands 2 to 4). The main difference is a higher reflectance of the class agriculture in band 2 to 4.

The spectral signature of “Water” shows higher reflection values around band 7 leading to the interpretation that the water class/signature contains impurities, such as sediments. Pure water would have zero reflectance in these longer wavelengths.

The spectral curve of the class “Urban” shows a relatively continuous increase. The spectral curve can be compared to the signature of “Bare Soil”, as both signatures show corresponding characteristics. The main difference between both spectral signatures is the intensity of reflectance.

Classification

To perform the supervised classification, the Maximum Likelihood classifier is selected. This method assumes a Gaussian (normal) distribution of the statistics of each class in each spectral band, and the assumption of a Gaussian distribution can be seen as generally reasonable for common spectral response distributions.

The probability of a pixel belonging to one of the above defined classes is calculated based on the mean vector of a class and the covariance matrix. According to the highest probability value, a pixel is assigned to a certain class (LILLESAND ET AL., 2015).

Post-Processing

The same object feature may be classified in different classes due to spectral variabilities. The classification result might show single isolated pixels of one class in the area of another class (LILLESAND ET AL., 2015).

To remove the single isolated pixels in the classification image, a sieve filter is applied. This filter replaces all pixel patches that are smaller than four pixels by the value of the surrounding neighbor class. A pixel patch is a group of pixels that share their sides or have connected angles. The final classification result is shown in Fig. A2 and A3.

Calculation of filled and non-filled areas

Based on the knowledge of the GSB colleagues and the experience gained during fieldwork, all urbanized areas and settlement structures in Kushtia are developed on filled areas. Therefore, those areas are considered as filled areas, the classes “Urban” and “Rural Settlements” are reclassified to “Filled” and the classes “Water”, “Bare Soil” and “Agriculture” are reclassified to “Non-filled” (see Fig. A4).

Accuracy Assessment

During the accuracy assessment, randomly distributed test samples are used to compare the classification result with an independent high-resolution reference dataset. As a high-resolution reference dataset, free accessible Google Earth satellite images are used. Thus, details for a more precise interpretation of the actual land use become visible and the classification result can be assessed visually without having the necessity to collect ground truth information during fieldwork.

LILLESAND ET AL. (2015) recommends using at least 50 test samples per class for accuracy assessment. Following this recommendation, 250 test samples are randomly distributed in the image, using 50 samples for each class (Tab. 3).

Table 3: Accuracy Assessment, Sentinel-2 dataset (22.09.2019).

Sentinel-2, 22.09.2019		Reference					Row Total	User's Accuracy (%)
		Agriculture	Bare Soil	Rural Settlements	Urban	Water		
Classification	Agriculture	47	0	3	0	0	50	94.0
	Bare Soil	16	31	1	1	1	50	62.0
	Rural Settlements	14	1	34	1	0	50	68.0
	Urban	7	4	6	31	2	50	62.0
	Water	0	0	2	0	48	50	96.0
	Column Total	84	36	46	33	51	250	
	Producer's Accuracy (%)	55.95	86.11	73.91	93.93	94.11		
	Cohen's Kappa per Class	0.89	0.61	0.63	0.58	0.94		
	Overall Accuracy (%)	76.4						
	Overall Kappa	0.8						

Since the images from Google Earth represent a compilation of different points in time, the Sentinel-2 dataset is used as an auxiliary dataset. Both data sets were acquired at different stages of flooding. Therefore, the visual impression of the Sentinel-2 dataset is given priority over the data from Google Earth when assigning water areas. Based on these datasets, land-use classes are interactively assigned to the test sample classes. Following this, the test areas are compared with the classification results to receive the accuracy measures (Tab. 3).

The overall accuracy of the classification is 76.4 %. The Kappa coefficient, a measure for the agreement between classification result and reference shows a good result of 0.8. The User's Accuracy shows how reliable the classified pixels represent actual land use, while Producer's Accuracy shows how well an object class has been correctly classified. In addition, the Kappa coefficients of each class are displayed in order to individually evaluate the reliability of the classification result.

The "Water" class is most reliably classified with a User's Accuracy of 96.0 %. A similarly high accuracy is achieved in the "Agriculture" class (User's Accuracy of 94.0 %). This is reflected in the high Kappa coefficients of 0.94 for "Water" and 0.89 for "Agriculture".

The "Rural Settlements" (68.0 %), "Urban" (62.0 %) and "Bare Soil" (62.0 %) classes also share a common, but lower range, in the User's Accuracy. This is also visible in the Kappa coefficients, so that the agreement between the classification result and the reference data is 0.61 ("Bare Soil"), 0.63 ("Rural Settlements") and 0.58 ("Urban"). The reason for these overall lower accuracy values may be related to different circumstances. For example, the spectral signature of the "Rural Settlements" class is very similar to the spectral signature of the "Agriculture" class and differs only in the first four bands by a lower intensity (Fig. 4). "Rural Settlements", that could have similar spectral characteristics like vegetable plantations, may therefore be classified incorrectly.

Tab. 3 also shows that a notable number of "Bare Soil" samples were classified as "Agriculture". This may be related to the different vegetation stages of the crops. Fields that are shortly before harvest have a similar signature as "Bare Soil" and may therefore be misclassified.

The relatively low accuracy value of the "Urban" class may be related to a mixed-pixel problem in the Sentinel-2 dataset. Individual residential or industrial buildings may be smaller than the resolution of the Sentinel-2 dataset (10m x 10m). As a result, a pixel represents a mixture of urban buildings and other surfaces (e.g. soil or trees). This mixture can lead to misclassification. Due to the high-resolution reference image, it is possible to interactively determine the main content of a pixel (e.g. urban buildings) and to assign it to the test sample classes. The mixed pixels of the Sentinel-2 dataset can thus lead to a lower accuracy in the "Urban" class.

The overall visual impression of the classification result (Fig. A2), as well as the overall accuracy and the overall Kappa coefficient (Tab. 3) show a good result and representation of the actual land-use.

2.2 River Shifting Change Detection Map

Rivers in Bangladesh are highly dynamic and underlie severe changes in location and intensity during a few years. During a few decades, rivers may change whole landscapes. The overall goal of this analysis is to provide information on the changes of the Padma river system course and the direction of shifting. The river system includes the water bodies and pointbars. A regional map covers these changes from the area of Bagha in the northwest to the area of Kumarkhali in the southeast (Fig. A6). Local changes inside this area are presented in a map showing only the city of Kushtia (Fig. A17). The focus is the mapping of recent active areas of the river system and passive areas which were active in the past decades but are inactive recently. River course maps are provided for six time slices (1973, 1980, 1990, 2000, 2010 and 2019) (Fig. A9-A14). The change detection map shows data of the time slices with the highest difference in river system areas (1973, 2000 and 2019) (Fig. A9-A14, A16). A map focusing on the Kushtia study area shows active and passive river system areas using all six time slices (Fig. A17).

Data

To carry out the analysis, cloud-free optical images from Landsat Multispectral Scanner System MSS, Landsat Thematic Mapper TM and Copernicus Sentinel-2 missions are used. These are available during the period of the Bangladesh dry season between October and April, and images from January and February are used in the analysis. A comparison between images of different years is only possible when the target features (e.g. water) can be identified in all the images by similar response signal. This can be ensured by using images of the same month in every year of the analysis.

Starting 1973, one image per decade is used (1973, 1980, 1990, 2000, 2010 and 2019).

To enable comparability between the final river shifting products, only bands from the Landsat and Copernicus Sensors with similar wavelengths positions have been chosen for processing (see Tab. 4 and Annexure C: Data).

Table 4: Overview of the satellite images and their bands used for the analysis (EUROPEAN SPACE AGENCY 2017; UNITED STATES GEOLOGICAL SURVEY n.d.).

Mission	Sensing Date	Bands (B), Spatial Resolution/ Wavelengths	
		Green	NIR
Landsat MSS	21.02.1973	B4, 60m 0.5-0.6 μm	B7, 60m 0.8-1.1 μm
	21.02.1980		
Landsat TM	13.01.1990	B2, 30m 0.52-0.6 μm	B4, 30m 0.76-0.90 μm
	11.02.2000		
	06.02.2010		
Sentinel-2	24.02.2019	B3, 10m 0.538-0.583 μm	B8, 20m 0.76-0.97 μm

Methods

The workflow of the analysis is visualized in Fig. 5.

Atmospheric Correction

Different atmospheric conditions during the sensing times of the images can result in a different image feature of the physically same ground objects. Therefore, to enable the comparison between all the images, an atmospheric correction is mandatory. An atmospheric correction eliminates the atmospheric effects in an image and results in a surface reflectance image that characterizes the surface properties. The Sentinel-2 image is atmospherically corrected by using the free available European Space Agency (ESA) Sen2Cor processor with three parameter changes from the default settings (see Tab. 5) (ESA, 2019).

The Sen2Cor algorithm is a correction method based on physical principals. Physical-based algorithms use radiative transfer methods, which are simplified models of the radiation pathway from source to sensor, to model atmospheric scattering and absorption (LILLESAND ET AL., 2015). Auxiliary data such as water vapor data, atmospheric pressure or a digital elevation model are added to receive more precise information for the correction. The effects in the atmosphere are quantified by the model and used to calculate the surface reflectance values.

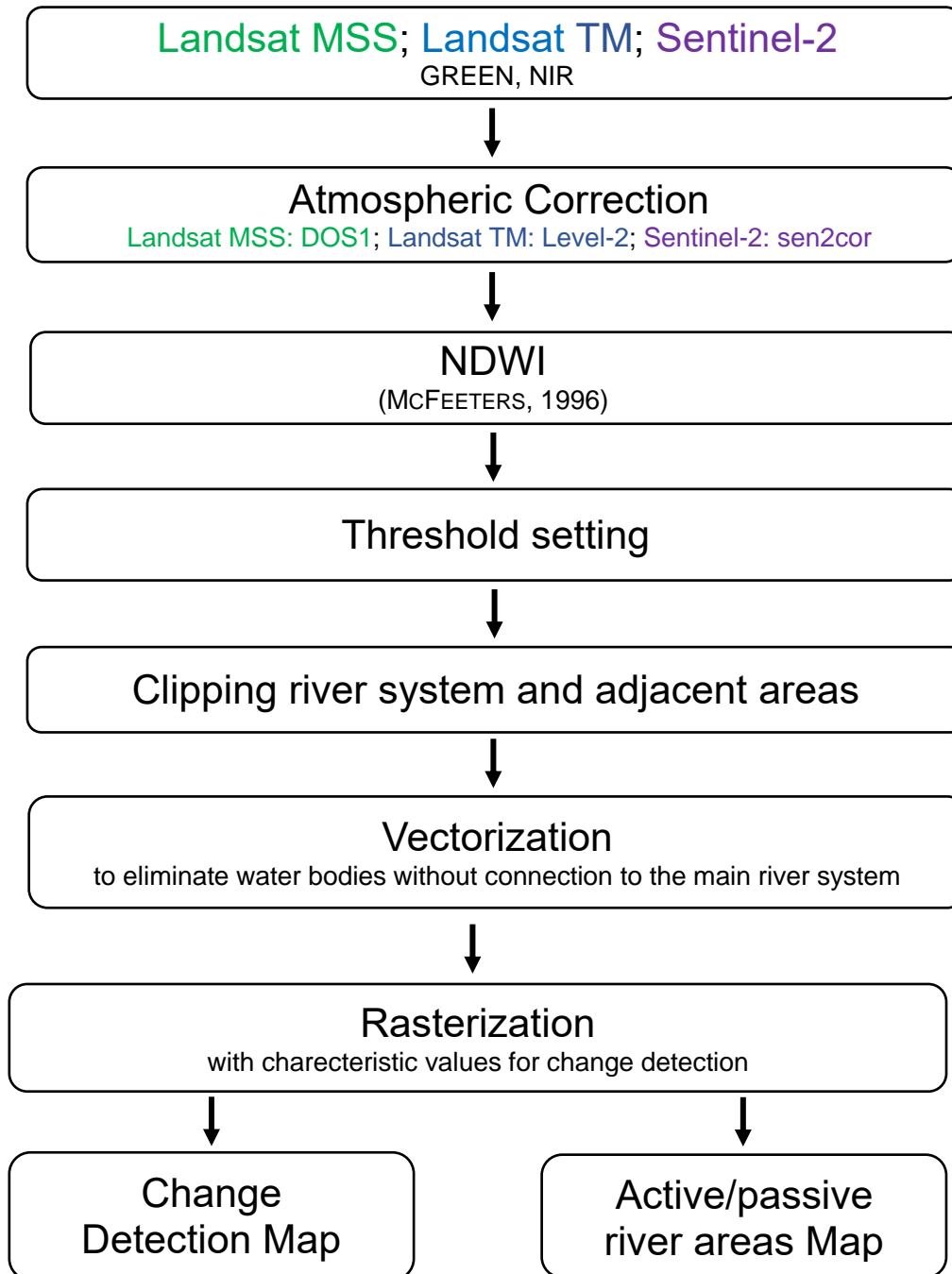


Figure 5: Workflows of the River Shifting Change Detection analysis.

Table 5: Overview of the parameters and setting changes for the atmospheric correction of Sentinel-2 data.

Parameter	Setting	Description
Mid_Lat	AUTO	Selection of atmospheric profile. If set to AUTO the processor will select WINTER or SUMMER based on acquisition date and geographic location. (MUELLER-WILM ET AL., 2018, p. 25)
Ozone	0	Ozone content: If option 0 is chosen it will be set by using the metadata and the Lookup-Tables. (MUELLER-WILM ET AL., 2018, p. 25)
DEM directory	<download directory>	Providing a directory activates the use of SRTM DEMs for topographic correction. (MUELLER-WILM ET AL., 2018, p. 33)

Landsat TM images are already atmospherically corrected available for download. The surface reflectance “products are generated by a specialized software called Landsat Ecosystem Disturbance Adaptive Processing System (LEDAPS)” (LEDAPS PRODUCT GUIDE, 2020). Similar to Sen2Cor, LEDAPS is also a physical-based algorithm that fits a radiative transfer model and includes auxiliary data to receive the atmospherically corrected surface reflectance product.

The Landsat MSS image is corrected by using the DOS1 (Dark Objects Subtraction) method. CHAVEZ (1996) describes that the methods “[...] basic assumption is that within the image some pixels are in complete shadow and their radiances [if above zero] received at the satellite are due to atmospheric scattering (path radiance). This assumption is combined with the fact that very few targets on the Earth’s surface are absolute black, so an assumed one-percent minimum reflectance is better than zero percent.” (CHAVEZ, 1996). The calculated radiance-value based on this assumption is used for the correction of the whole Landsat MSS image (image –based correction).

It is important to mention that the accuracy of an image-based correction technique is lower than a physically based correction (e.g. as applied for Sentinel-2) (CONGEDO, 2016). Nevertheless, CONGEDO (2016) states that image-based corrections “are very useful when no atmospheric measurements are available as they can improve the estimation of land surface reflectance” (CONGEDO, 2016).

Calculation of Normalized Difference Water Index (NDWI)

Using the respective bands of the images (Tab. 4), the NDWI is calculated (see Fig. A7). The Normalized Difference Water Index (NDWI) (McFEETERS, 1996) uses the green and near-infrared bands to delineate open-water features. Water surfaces show high reflections in the green and low reflections in the near-infrared wavelength region (see Fig. 5).

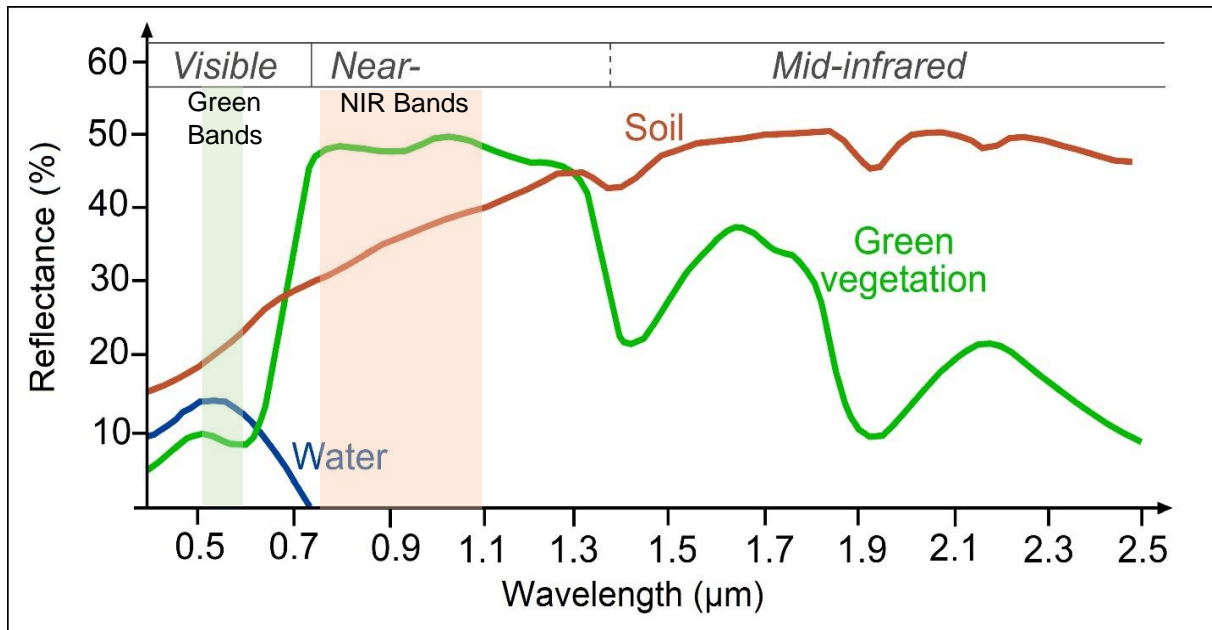


Figure 6: Reflectance of water, soil and vegetation at different wavelengths; the wavelength areas used by the NDWI are highlighted in green (green bands) and red (NIR bands), modified after SEOS-PROJECT.EU, 2020.

These differences are used to calculate an index that enhances the presence of open water features and suppresses the presence of soil and vegetation (MCFEETERS, 1996). The Waterindex is calculated as follows, using the respective bands of the satellite image:

$$NDWI = \frac{GREEN - NIR}{GREEN + NIR}$$

The generated index map contains values in the range of -1 to +1 (see Fig. A7), while excluding zero. Positive values are interpreted as water features. Soil and vegetation features have negative values (MCFEETERS, 1996).

Processing steps

At first, a threshold value is applied to discriminate between values that belong to the river system (water-bodies and pointbars) and all other values. This threshold value is defined manually by inspecting the pixels of the different NDWI images (see Tab. 6).

Table 6: Thresholds to discriminate between river system and other values.

NDWI image of the year	Threshold
1973	-0.26
1980	-0.05
1990	-0.25
2000	-0.15
2010	-0.18
2019	-0.15

The application of the thresholds results in maps that only show water-body and pointbar areas differentiated from other areas (see Fig. A8 as an example).

Based on these threshold maps, an area is clipped interactively (due to computing limitations of QGIS regarding data quantity) that covers mainly the river system (including water bodies and pointbars) and adjacent areas. In the next step, all remaining pixels of the river system in the clipped images are assigned the value “1”, whereas the areas below the threshold (see Tab. 6) are assigned NA.

The resulting image still includes many small objects that lie outside of the main riversystem (e.g. small ponds, agricultural canals). To eliminate these water bodies having no connection to the main river system, the raster data are vectorized and single isolated polygons are automatically eliminated, based on the assumption that the main river area shows in one connected polygon.

The results of all processed years are overlain to visualize the different extents (Fig. A9-A14). The three results with the greatest differences in extent are selected interactively and then processed for the change detection map: years 1973, 2000 and 2019 (Fig. A16).

Change Detection Map

The goal of the change detection map is to provide information on the changes of the Padma river system course and the direction of shifting. The changes are visualized in a single map. The conversion of the vector map (polygons) back to a raster map enables to present different river areas with characteristic values in a single map.

A unique year-dependent characteristic value is assigned to the cells of each new raster image (see Tab. 7). The raster cell size is set to 20 m, as this is the pixel size, needed by the successive project analyses.

The yearly products are joined to receive the change detection map of the area of the Padma river system for the different years (see Tab. 8).

Table 7: Overview of the characteristic values per year.

	1973	2000	2019
Characteristic value	1	10	100

Table 8: Legend of the raster values in the change detection map.

Raster value	Area of the Padma river system in
1	1973
10	2000
11	1973, 2000
100	2019
101	1973, 2019
110	1973, 2000
111	1973, 2000, 2019

Mapping active and passive river system areas

In the Kushtia study area, the information of all results (1973, 1980, 1990, 2000, 2010, 2019) are included into a map that presents active and passive areas of Padma river system.

Active areas are defined as the area of the Padma river system in 2019.

Passive areas are defined as the area of the Padma river system in all years before 2019 but not in 2019.

The polygons of each year are rasterized. A unique year-dependent characteristic value is assigned to the cells of each new raster image (see Tab. 9). The raster cell size is set to 20 m, as this is the pixel size, needed by the successive project analyses.

The individual results are joined. The values of the map represent the area of the Padma river system in different years (see Tab. 10). To reduce the values to active or passive areas, the raster is reclassified into two classes (see Tab. 10).

Areas where the river is not classified in 2019, are defined as passive and are assigned with a value of “1”. Areas, which show the river system in 2019, are defined as active and are assigned with the value of “2”.

Table 9: Overview of the characteristic values per year for the mapping of active/passive river system areas.

	1973	1980	1990	2000	2010	2019
Characteristic value	1	10	100	1000	10000	100000

Table 10: Legend of the raster cell values in the map of active/passive river system areas.

Characteristic value	Area of the Padma river system in	Reclassified value (1=passive/2=active)
1	1973	1
10	1980	1
11	1973, 1980	1
100	1990	1
101	1973, 1990	1
110	1980, 1990	1
111	1973, 1980, 1990	1
1000	2000	1
1001	1973, 2000	1
1010	1980, 2000	1
1011	1973, 1980, 2000	1
1100	1990, 2000	1
1101	1973, 1990, 2000	1
1110	1980, 1990, 2000	1
1111	1973, 1980, 1990, 2000	1
10000	2010	1
10001	1973, 2010	1
10010	1980, 2010	1
10011	1973, 1980, 2010	1

10100	1990, 2010	1
10101	1973, 1990, 2010	1
10110	1980, 1990, 2010	1
10111	1973, 1980, 1990, 2010	1
11000	2000, 2010	1
11001	1973, 2000, 2010	1
11010	1980, 2000, 2010	1
11011	1973, 1980, 2000, 2010	1
11100	1990, 2000, 2010	1
11101	1973, 1990, 2000, 2010	1
11110	1980, 1990, 2000, 2010	1
11111	1973, 1980, 1990, 2000, 2010	1
100000	2019	2
100001	1973, 2019	2
100010	1980, 2019	2
100011	1973, 1980, 2019	2
100100	1990, 2019	2
100101	1973, 1990, 2019	2
100110	1980, 1990, 2019	2
100111	1973, 1980, 1990, 2019	2
101000	2000, 2019	2
101001	1973, 2000, 2019	2
101010	1980, 2000, 2019	2
101011	1973, 1980, 2000, 2019	2
101100	1990, 2000, 2019	2
101101	1973, 1990, 2000, 2019	2
101110	1980, 1990, 2000, 2019	2
101111	1973, 1980, 1990, 2000, 2019	2
110000	2010, 2019	2
110001	1973, 2010, 2019	2
110010	1980, 2010, 2019	2
110011	1973, 1980, 2010, 2019	2
110100	1990, 2010, 2019	2

110101	1973, 1990, 2010, 2019	2
110110	1980, 1990, 2010, 2019	2
110111	1973, 1980, 1990, 2010, 2019	2
111000	2000, 2010, 2019	2
111001	1973, 2000, 2010, 2019	2
111010	1980, 2000, 2010, 2019	2
111011	1973, 1980, 2000, 2010, 2019	2
111100	1990, 2000, 2010, 2019	2
111101	1973, 1990, 2000, 2010, 2019	2
111110	1980, 1990, 2000, 2010, 2019	2
111111	1973, 1980, 1990, 2000, 2010, 2019	2

Results and Discussion

The resulting maps are added in Annexure A (A6-A17) and described in this section. For better orientation, topographical information and some in Bangladesh well-known cities are included in the final map visualization of the remote sensing based products.

Extent of Padma river system and its water body

As already mentioned, the NDWI values greater than the threshold lead to the classification of a larger area than just the water bodies as it includes water bodies and pointbars. All together is interpreted as full extent (maximum water coverage) of the Padma river system based on discussions with the GSB colleagues. As an example, Figure A10 shows the NDWI result for 2010 with a threshold greater than -0.18 overlain on the Landsat TM RGB 321 image from 2010. It is visible that the water body, pointbars, as well as some brownish vegetated areas – the floodplain – are included into the result.

Fig. A9 to A14 show in blue the extents of the Padma river system (based on NDWI) in the years of 1973, 1980, 1990, 2000, 2010 and 2019.

The different levels of details between the final maps are caused by the different spatial resolutions of the images. Due to the higher spatial resolution, Sentinel-2 shows more details than Landsat TM and Landsat MSS (Tab. 4).

It can be summarized, that the general shape of river system for the different years is visible in all decades.

Change Detection Map

Based on the NDWI evaluations, the change detection map is calculated (Fig. A16). This map includes information on the shifting direction of the river system, together with the locations of land-loss and possible land-gain. Furthermore, it shows which regions were part of the river system for the period between 1973 and 2019 (Fig. A16, dark blue).

In several regions of the river areas, changes in time are observable (Fig. A16): Southeast of Bheramara, a progressing cut bank is clearly visible:

Dark blue color shows the extension of the river system in the years of 1973, 2000 and 2019, orange color the extension of the river system in the years of 2000 and 2019. The red color represents areas of the river system in the year of 2019. The change detection map visualizes a relocation of the river system to the southeastern direction. A similar river relocation is visible west of Ishwardi: Light green color shows the position of the river system in 1973 and 2000, light orange in 2000. The darker orange and red color represent the position of the river system in 2000 and 2019, showing a shift of the river system to the northwest. Areas in light green, light blue and turquoise are not part of the river system since 2000; an increased vegetation and therefore possible anthropogenic use like agriculture support this interpretation.

In contrast, northeast of Kumarkhali an area of light green, light blue and turquoise colors is visible. The change detection map indicates that this region was part of the river system from 1973 until 2000, but not in 2019. Therefore, these areas can be interpreted as a retreat of the river system to the north. A similar development is visible on the northern side of the Padma River between Rooppur and Pabna. The turquoise color indicates large areas where the river extended only in 1973, whereas the light green and light orange color in this region indicate a retreat of the river system in the southwest.

In summary, the area between Bheramara and Pabna shows the shape of a meander bow. The retreat of the river system on the sedimentation side of the meander bow south of Rooppur corresponds with the evolving erosion bank southeast of Bheramara. In this region, the river developed from 1973 to 2019 into the southeastern direction. In other regions, only little changes over the period of 46 years are visible, especially on the southern riverbank northwest of Kumarkhali.

A possible explanation could be an anthropogenic embankment along the riverbank. A similar region is visible north of the Lalon-Shah-Bridge showing only very little changes.

It is also noteworthy that from 1973 to 2019 the Garai River at Kushtia shifted towards the east.

Overall, the Change Detection Map in Fig. A16 shows that the general river system is regionally stable, but changes a lot on a local scale.

Active and passive river areas in Kushtia study area

In the Kushtia study area, the change detection map shows active and passive areas (Fig. A17). The map allows locating areas of sedimentation processes (passive areas) and provides indications on other geo-related processes (e.g. liquefaction-prone areas).

2.3 Inundation Map

Due to climate change, Bangladesh is experiencing an increase in rural-urban migration movements. Therefore, the demand for safe building ground is very high. One result is an increasing lateral growth of urban areas. However, urban growth is limited to suitable building ground and eligible areas are often low-lying and therefore prone to flooding during the yearly monsoon season between May and October. Planning agencies may benefit from geodata on inundation-prone areas that are reliable, available frequently and sustainable, easy to process and easily understandable.

The overall objective of this analysis is to receive a map that gives an overall impression on the frequency of inundation in areas that are at risk of flooding (Fig. A18) for the years 2015 to 2020. The analysis is carried out using 51 Sentinel-1 radar images from 2015 to 2020 and a threshold approach to differentiate between inundated and non-inundated areas. To ensure an easy processing of the large amount of multi-temporal radar data, the analysis is carried out using the online processing tool Google Earth Engine (see the Google Earth Engine code in Annexure B).

The Bangladesh Water Development Board (BWDB) already established inundation mapping using Sentinel-1 datasets. In their annual flood reports, the BWDB is using an inundation map to verify the output of a flood-forecasting model (BANGLADESH WATER DEVELOPMENT BOARD, 2018, pp. 92-93).

Data

The analysis is based on Copernicus Sentinel-1 images starting 2015, with operation of the Sentinel 1 sensor.

Google Earth Engine states to preprocess the images using the Sentinel-1 Toolbox to receive radiometrically calibrated images, terrain corrected and thermal noise removed (GOOGLE EARTH ENGINE DATA CATALOG, 2020).

A data selection from the rainy season in Bangladesh is required to map the maximum inundation. The selected images are acquired in “IW” (interferometric wide swath), the default acquisition mode of Sentinel-1 (EUROPEAN SPACE AGENCY, 2020). To differentiate between water and non-water pixels, the VH polarization (vertical transmit of the signal and horizontal receive of the signal) is selected. Preliminary works in the study areas have shown that VH is the most suitable polarization for the detection of water. The respective spatial resolution of the VH polarization images is 10 meter.

The Bangladesh rainy season is roughly between May and October of each year. Based on the experience and knowledge of colleagues of the Geological Survey of Bangladesh (GSB), the time of maximum inundation for the study area of Kushtia is set to the months of June and July of each year. Since the exact dates of maximum inundation of a year are unknown, all available images of June and July of each year are processed in this analysis.

Finally, using the above-mentioned benchmarks, 51 Sentinel-1 images of descending orbits are selected for the processing (Annexure B, lines 8-23). Annexure C: Data lists the images in a table.

Method

The workflow of the processing in Google Earth Engine is visualized in Fig. 7. The selected images of each year are combined and mean values are calculated. The mean-value images are subsetting to fit the extent of the study area (see Fig. A19; Annexure B, lines 24-29).

Thresholding

Water surfaces appear in black and dark gray colors in the averaged amplitude images (see Fig. A19). In order to identify a threshold value, the values of assumed water and non-water image areas are identified interactively.

Based on experience in the definition of thresholds discriminating between water and non-water surfaces, the identified threshold values in Bangladesh range from -20 dB to -22 dB. For the Kushtia study area, a threshold value including values smaller than -21 dB is chosen and applied to images from all years (Annexure B, lines 109-118). The output image only shows pixels smaller than the threshold, representing the inundated areas of each year (see Fig. A20 for the inundated areas of 2020).

All areas that have been flooded between 2015 and 2020, are compiled by combining the threshold images of all years into one image (see Fig. A18; Annexure B, lines 121-123). The result is exported with a 20m spatial resolution, which is a requirement for further analyses in the project (Annexure B, lines 129-141).

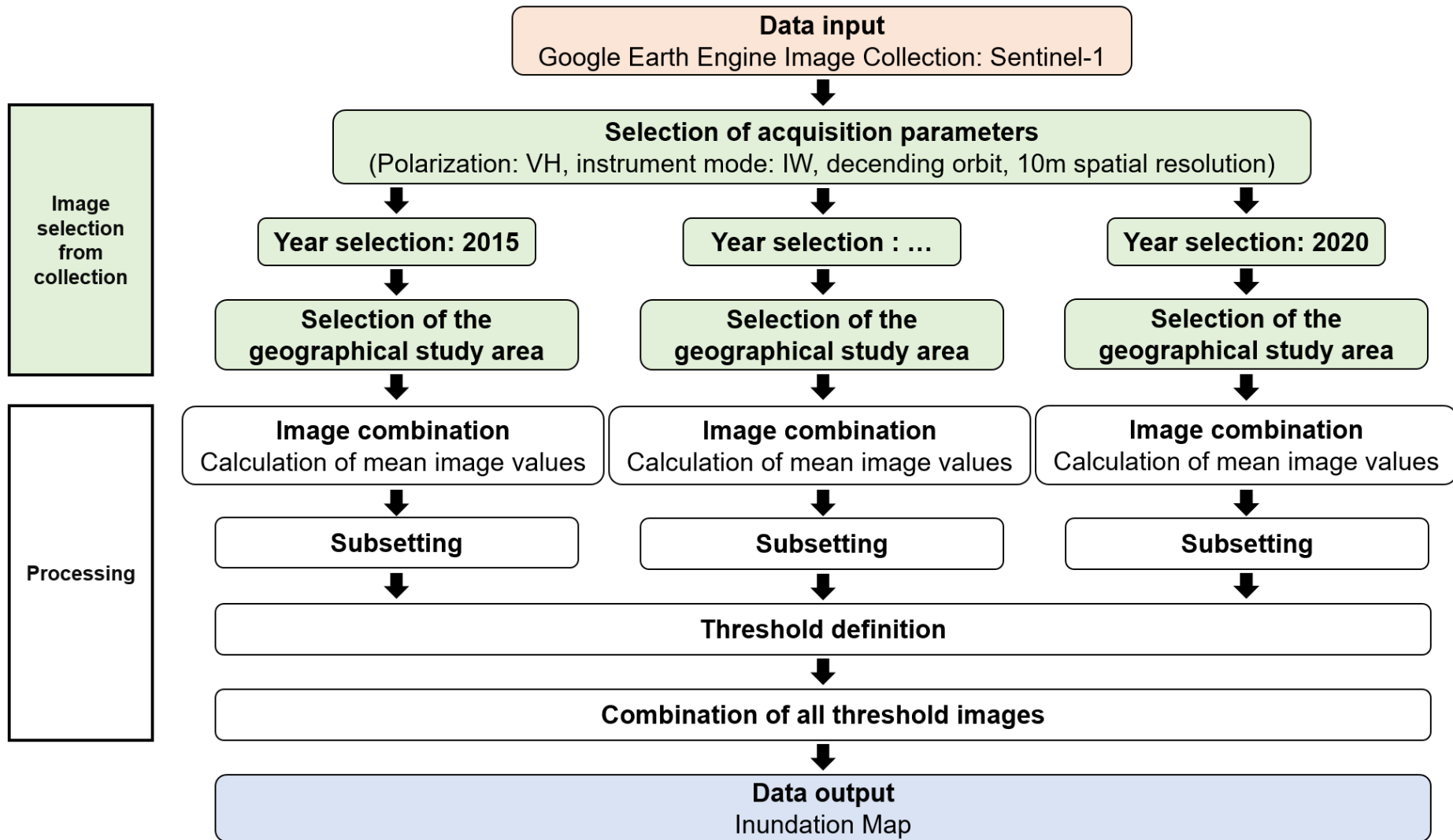


Figure 7: Workflow of the Google Earth Engine processing of the inundation mapping method.

Results and Discussion

The resulting map presents the areas and frequencies of inundation between 2015 and 2020 (see Fig. A18). The map exhibits three major inundation areas: Areas near the river, ponds and stagnant water bodies and inundated agricultural fields.

The areas near the river are located in close proximity to the Garai River that is bordering the northern part of the study area of Kushtia. Between the Jagia Uttarpara landmark and the Garai River, an area is located that is inundated almost every year during the six-year period investigated, whereas the areas facing the landmark are inundated less regularly. The high frequency of inundation from 2015 to 2020 implies to consider this area as part of the Padma river system during the rainy season (see chapter 2.2 River Shifting Change Detection for similar results).

Many small areas in the Kushtia city area are inundated yearly, representing ponds and lakes as they partially overlap with the water bodies in the topographic base map (data of the Survey of Bangladesh and OpenStreetMap).

The rural areas in the western part of the investigated area are clearly separable from the city (see Fig. A19) but, according to Fig. A18, only once or twice inundated during the six-year period.

However, there is a possibility that the areas west of the city of Kushtia have annual inundation at different locations instead of one frequently inundated large location.

It can be concluded that between 2015 and 2020 for the months June and July (rainy season) only areas near the river Garai are inundated. The inland-lying areas do not experience a high frequency of yearly area-wide flooding.

References

- BANGLADESH WATER DEVELOPMENT BOARD (2018):** Annual Flood Report 2018. – <http://www.ffwc.gov.bd/images/annual18.pdf>. (Last change: n.d.). (Last access: 16.12.2020).
- CHAMBELL J. B. (1996):** Introduction to Remote Sensing. 2nd edition. Taylor & Francis. London.
- CHAVEZ, P. S. (1996):** Image-Based Atmospheric Corrections - Revisited and Improved. Photogrammetric Engineering and Remote Sensing. Vol. 62. No. 9. 1025-1036.
- CONGEDO, L. (2016):** Semi-Automatic Classification Plugin Documentation. – <http://dx.doi.org/10.13140/RG.2.2.29474.02242/1>. (Last change: n.d.). (Last access: 08.08.2019).
- EUROPEAN ENVIRONMENT AGENCY (2017):** Copernicus Land Service – Pan-European Component: CORINE Land Cover. https://land.copernicus.eu/user-corner/publications/clc-flyer/at_download/file. (Last change: n.d.). (Last access: 22.01.2021).
- EUROPEAN ENVIRONMENT AGENCY (2019):** Updated CLC illustrated nomenclature guidelines. - https://land.copernicus.eu/user-corner/technical-library/corine-land-cover-nomenclature-guidelines/docs/pdf/CLC2018_Nomenclature_illustrated_guide_20190510.pdf. (Last change: n.d.). (Last access: 22.01.2021).
- EUROPEAN SPACE AGENCY (2017):** Sentinel-2 Spectral Response Functions (S2-SRF). – https://earth.esa.int/web/sentinel/user-guides/sentinel-2-msi/document-library/-/asset_publisher/Wk0TKajilSaR/content/sentinel-2a-spectral-responses. (Last change: 19.12.2017). (Last access: 13.06.2019).
- EUROPEAN SPACE AGENCY (2019):** Sen2Cor Configuration and User Manual V2.8. – <http://step.esa.int/thirdparties/sen2cor/2.8.0/docs/S2-PDGS-MPC-L2A-SUM-V2.8.pdf>. (Last change: 05.02.2019). (Last access: 22.08.2019).
- EUROPEAN SPACE AGENCY (2020):** Sentinel-1 User Guide: Interferometric Wide Swath. <https://sentinel.esa.int/web/sentinel/user-guides/sentinel-1-sar/acquisition-modes/interferometric-wide-swath>. (Last change: n.d.). (Last access: 16.12.2020).
- FORNARO, G., PASCAZIO, V. (2014):** Chapter 20 - SAR Interferometry and Tomography: Theory and Applications. Academic Press Library in Signal Processing. Vol. 2. 1043-1117. doi: 10.1016/B978-0-12-396500-4.00020-X.

GOOGLE EARTH ENGINE DATA CATALOG (2020): Sentinel-1 SAR GRD: C-band Synthetic Aperture Radar Ground Range Detected, log scaling. – https://developers.google.com/earth-engine/datasets/catalog/COPERNICUS_S1_GRD>. (Last change: n.d.). (Last Access: 16.12.2020).

LILLESAND, T. M., KIEFER, W., CHIPMAN, J. W. (2015): Remote Sensing and Image Interpretation. Seventh Edition. Wiley.

MCFEETERS, S. K. (1996): The use of the Normalized Difference Water Index (NDWI) in the delineation of open water features. International Journal of Remote Sensing. Vol. 17. No. 7. 1425-1432.

MOREIRA, A., PRATS-IRAOLA, P., YOUNIS, M., KRIEGER, G., HAJNSEK, I., AND PAPATHANASSIOU, K. P. (2013): A tutorial on synthetic aperture radar. In: IEEE Geoscience and Remote Sensing Magazine. Vol. 1, No. 1. 6-43. doi: 10.1109/MGRS.2013.2248301.

MUELLER-WILM, U., DEVIGNOT, O., PESSIOT, L. (2018): Level 2A Input Output Data Definition (IODD) v2.5.5. – <https://step.esa.int/thirdparties/sen2cor/2.5.5/docs/S2-PDGS-MPC-L2A-IODD-V2.5.5.pdf>>. (Last change: 23.03.2018) (Last access: 20.05.2019).

PRASAD S., BRUCE L. M., CHANUSSOT J. (2011): Introduction. Optical Remote Sensing. Augmented Vision and Reality, Vol. 3. Springer. Berlin, Heidelberg.

Rencz A. N. (1999): Manual of Remote Sensing. 3rd edition, Vol. 3. Remote Sensing for the Earth Sciences. John Wiley & Sons.

RICHARDS, J. A. (2009): Remote Sensing with Imaging Radar. Springer-Verlag. Berlin, Heidelberg.

SABINS F. F. (1996): Remote Sensing. 3rd edition. Freeman and Company. New York.

UNITED STATES GEOLOGICAL SURVEY (n.d.): What are the band designations for the Landsat satellites? – <https://www.usgs.gov/faqs/what-are-band-designations-landsat-satellites>>. (Last change: n.d.). (Last access: 13.06.2019).

UNITED STATES GEOLOGICAL SURVEY (2020): Landsat 4-7 Surface Reflectance (LEDAPS) Product Guide. Version 3.0. August 2020. – https://prd-wret.s3.us-west-2.amazonaws.com/assets/palladium/production/atoms/files/LSDS-1370_L4-7_C1-SurfaceReflectance-LEDAPS_ProductGuide-v3.pdf>. (Last change: August 2020). (Last access: 02.11.2020).

USTIN S. L. (2004): Manual of Remote Sensing. 3rd edition, Vol. 4. Remote Sensing for Natural Resource Management and Environmental Monitoring. John Wiley & Sons.

WOODHOUSE, I. H. (2006): Introduction to Microwave Remote Sensing. 1st edition. CRC Press. Boca Raton.

Annexure A: Maps

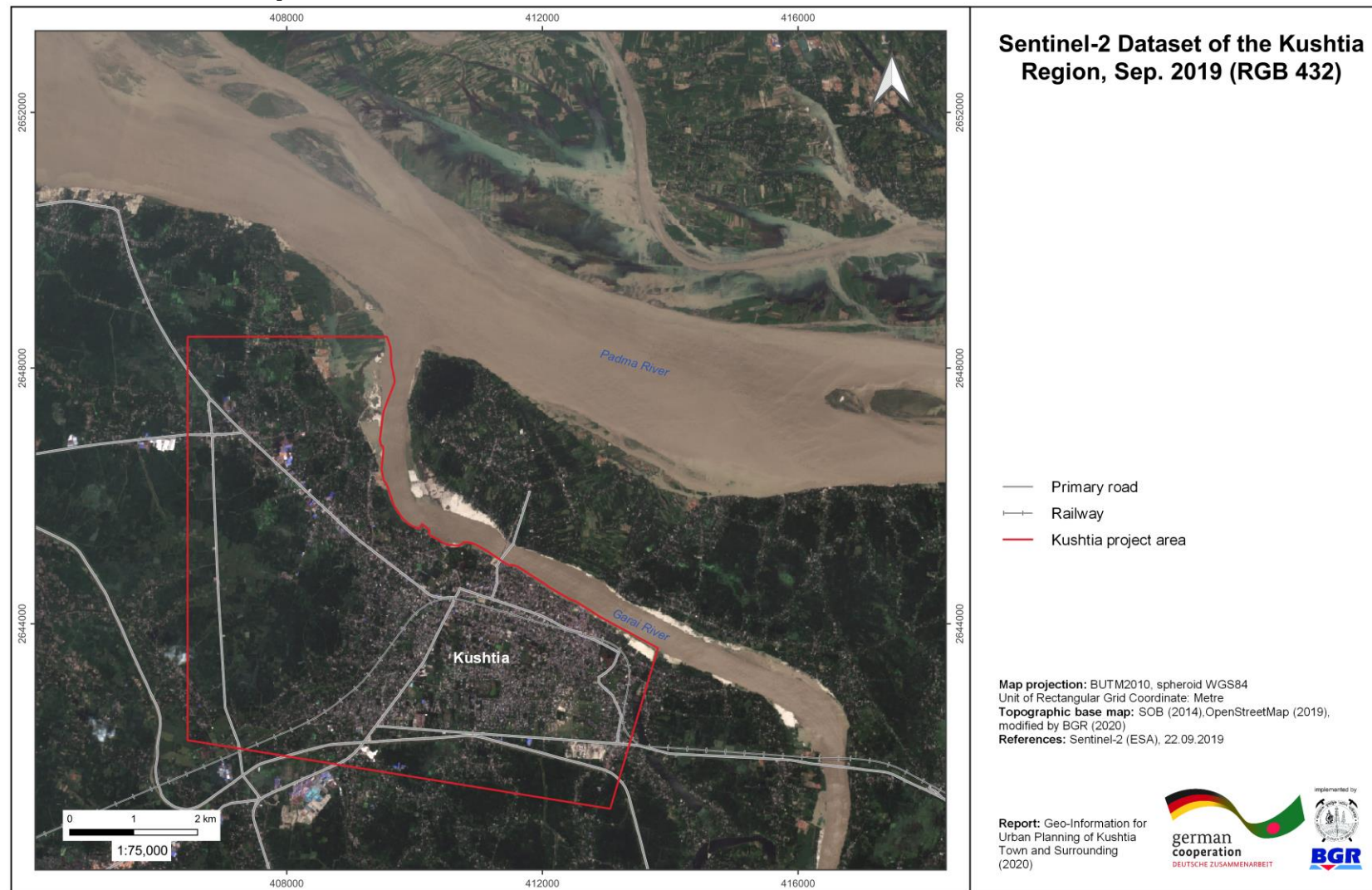


Figure A1: Sentinel-2 Dataset of the Kushtia Region, 22.09.2019 (RGB 4-3-2).

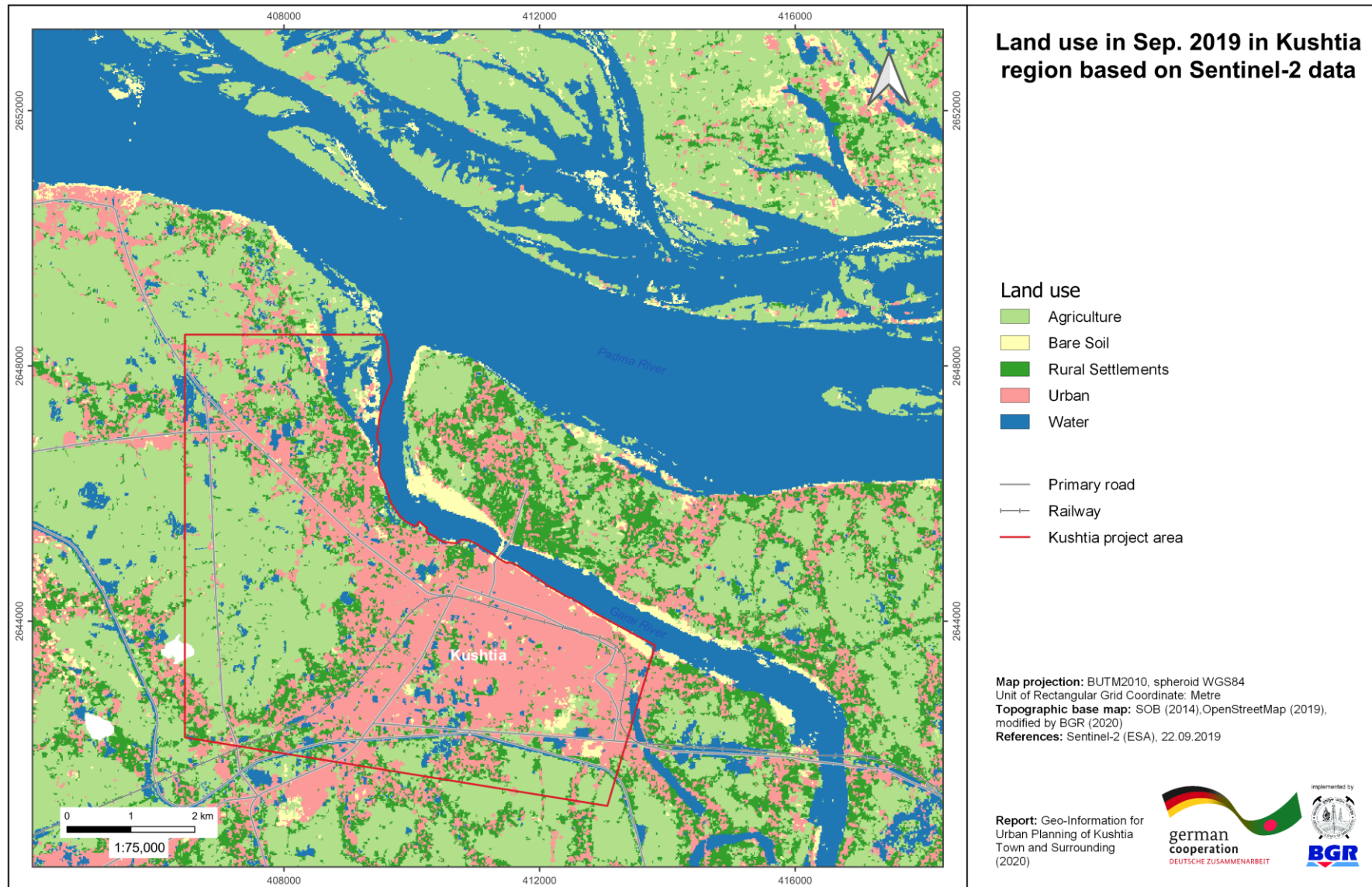
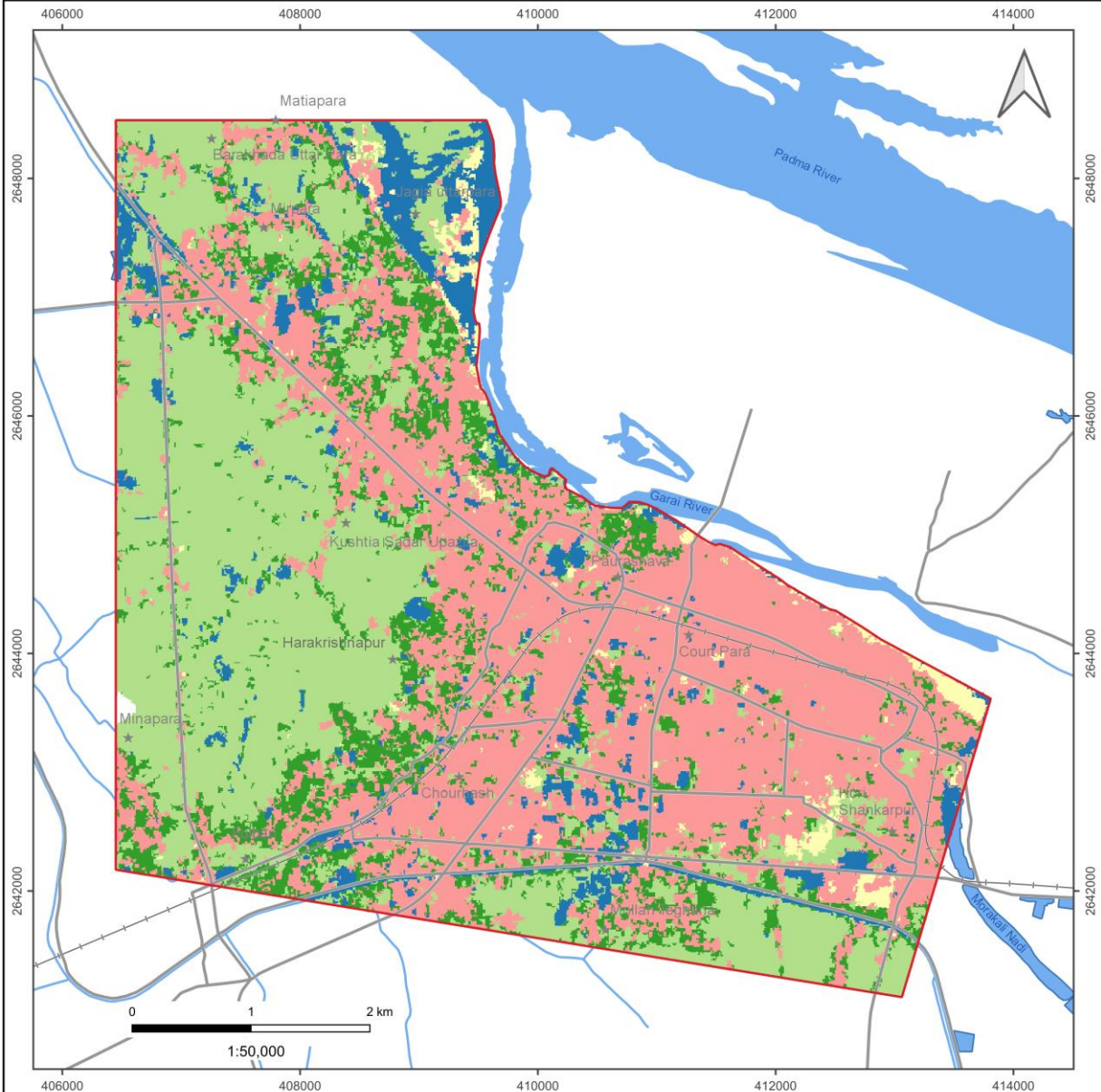


Figure A2: Land use in September 2019 in Kushtia region based on Sentinel-2 data.

Land use in Sep. 2019 in Kushtia project area based on Sentinel-2 data



Land use

- Agriculture
- Bare Soil
- Rural Settlements
- Urban
- Water

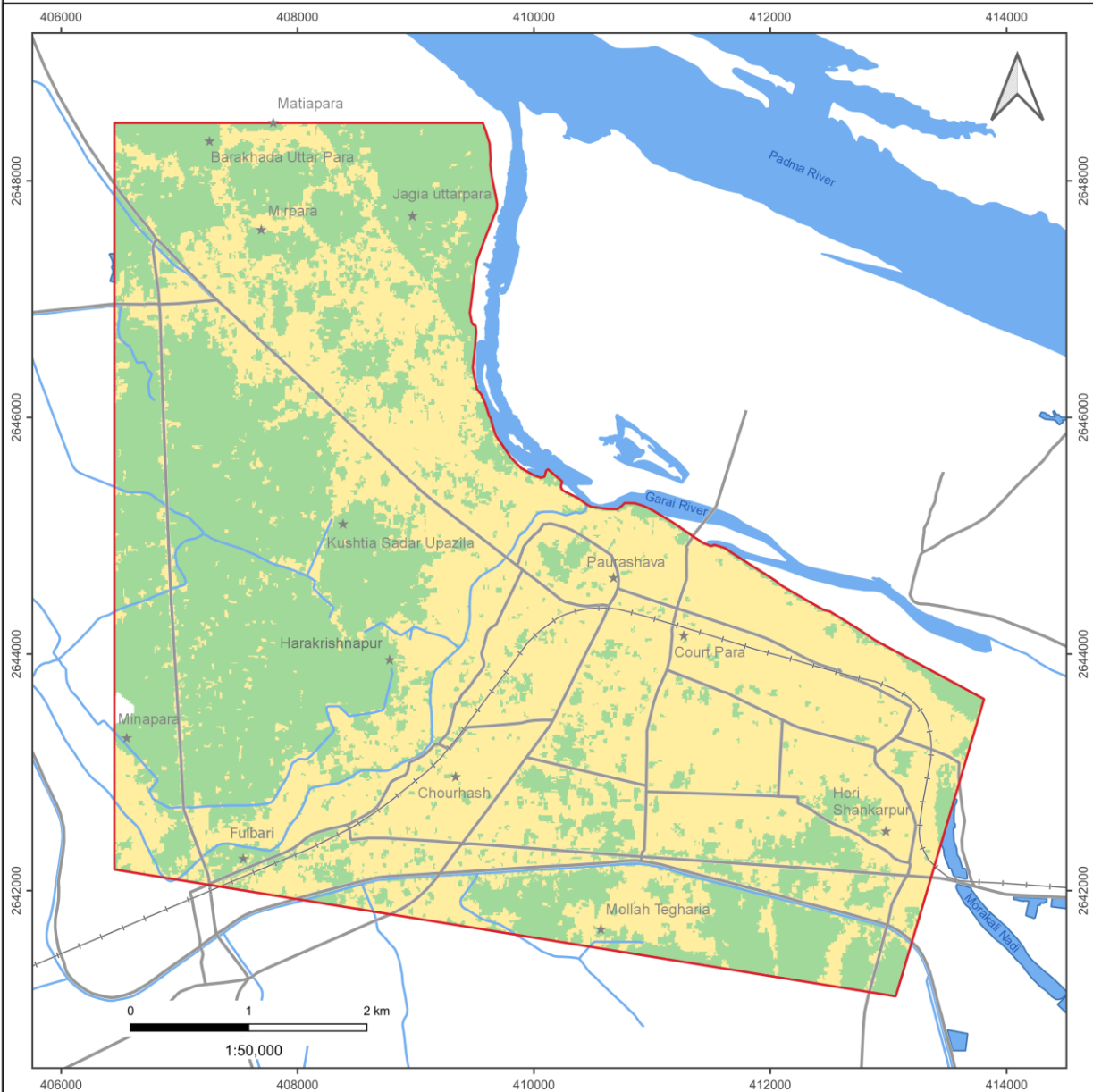
- ★ Landmark
- Primary road
- +— Railway
- ~ River
- Stagnant water >10.000 m²
- Canal
- Kushtia project area

Map projection: BUTM2010, spheroid WGS84
 Unit of Rectangular Grid Coordinate: Metre
Topographic base map: SOB (2014), OpenStreetMap (2019),
 modified by BGR (2020)
Reference: Sentinel-2 (ESA), 22.09.2019

Report: Geo-Information for Urban Planning
 of Kushtia Town and Surrounding (2020)

Figure A3: Land use in September 2019 in Kushtia project area based on Sentinel-2.

Status of Urban Development in Sep. 2019 in Kushtia project area based on Sentinel-2 data



Urban Development

- Filled
- Non-Filled

- ★ Landmark
- Primary road
- +— Railway
- River
- Stagnant water >10.000 m²
- Canal
- Kushtia project area

Map projection: BUTM2010, spheroid WGS84
 Unit of Rectangular Grid Coordinate: Metre
Topographic base map: SOB (2014), OpenStreetMap (2019),
 modified by BGR (2020)
Reference: Sentinel-2 (ESA), 22.09.2019

Report: Geo-Information for Urban Planning
 of Kushtia Town and Surrounding (2020)

Figure A4: Status of Urban Development in Sep. 2019 in Kushtia project area.

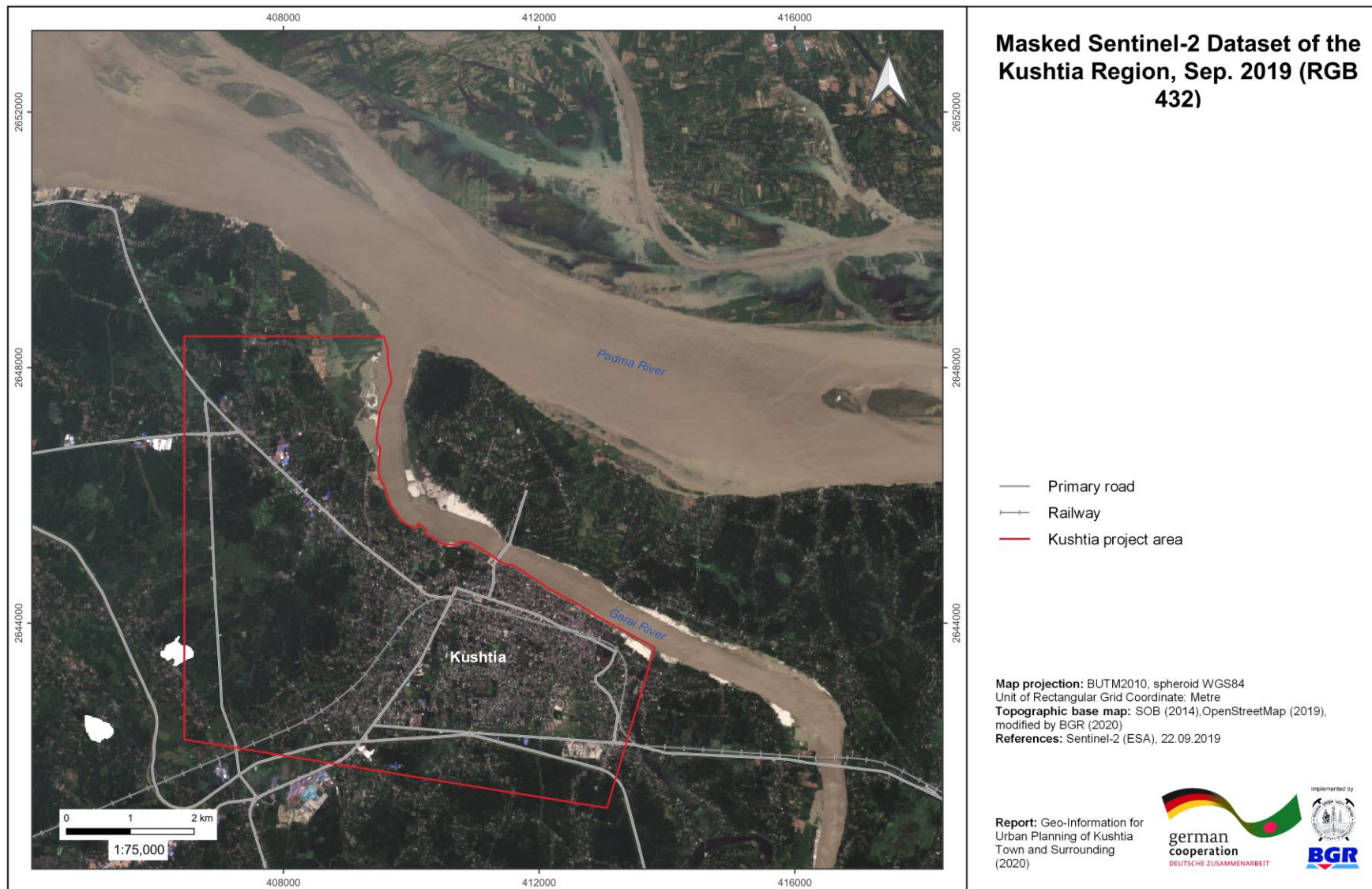


Figure A5: Masked Sentinel-2 Dataset of the Kushtia Region, September 2019 (RGB 4-3-2).

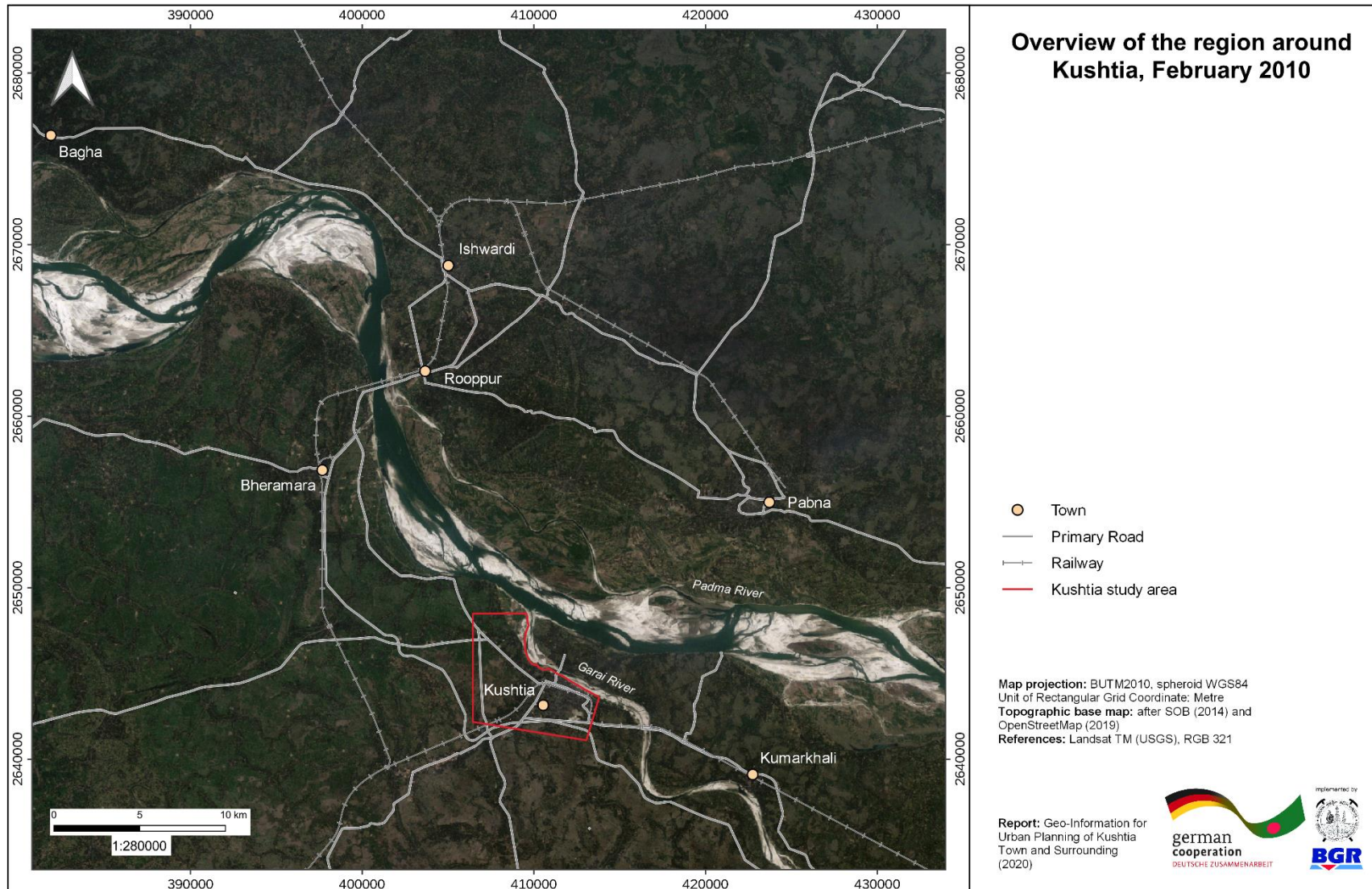


Figure A6: Overview of the region around Kushtia (Landsat TM, RGB 321, 06.02.2010).

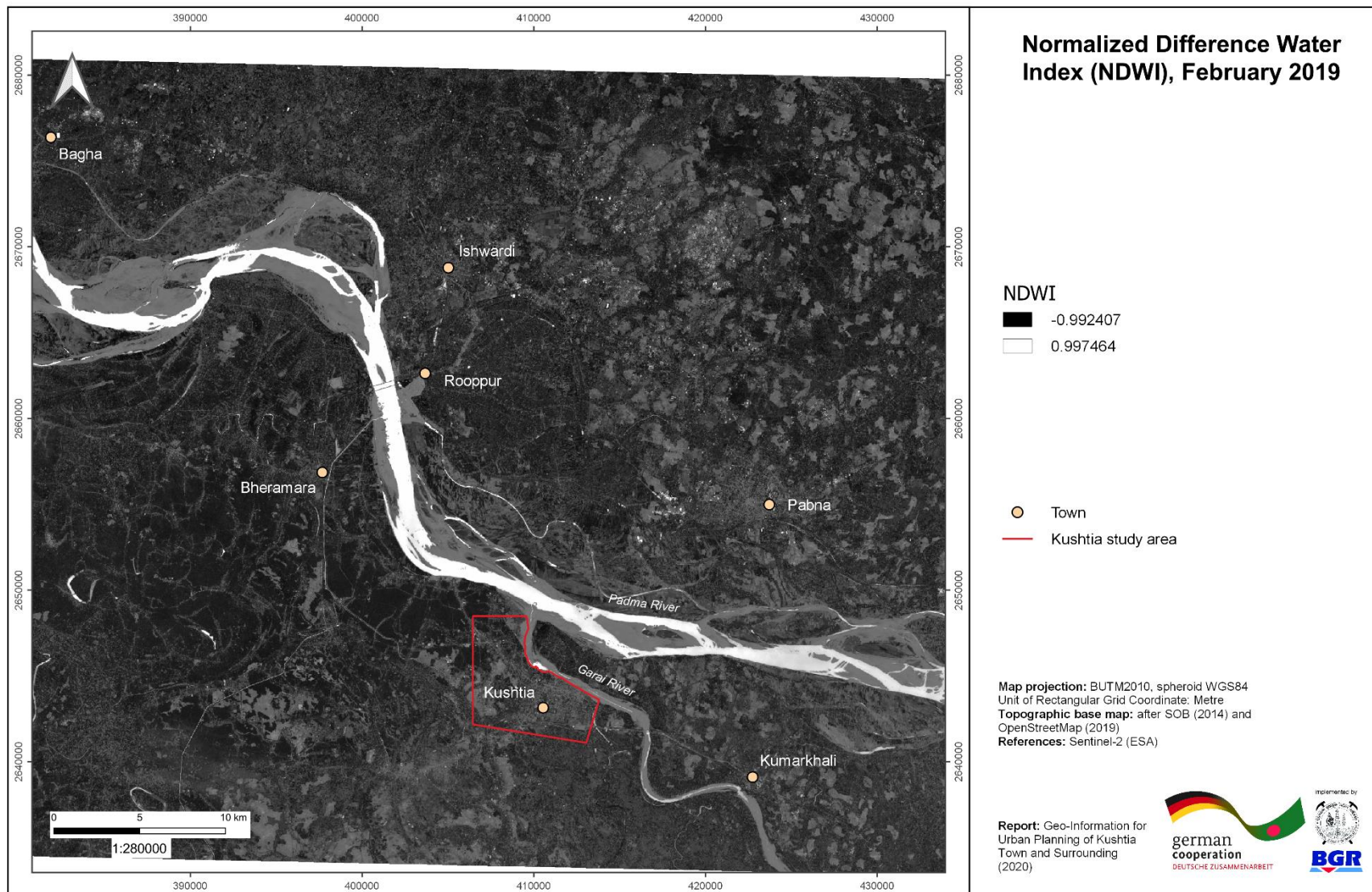


Figure A7: Normalized Difference Water Index (NDWI), based on Sentinel-2 imagery (24.02.2019).

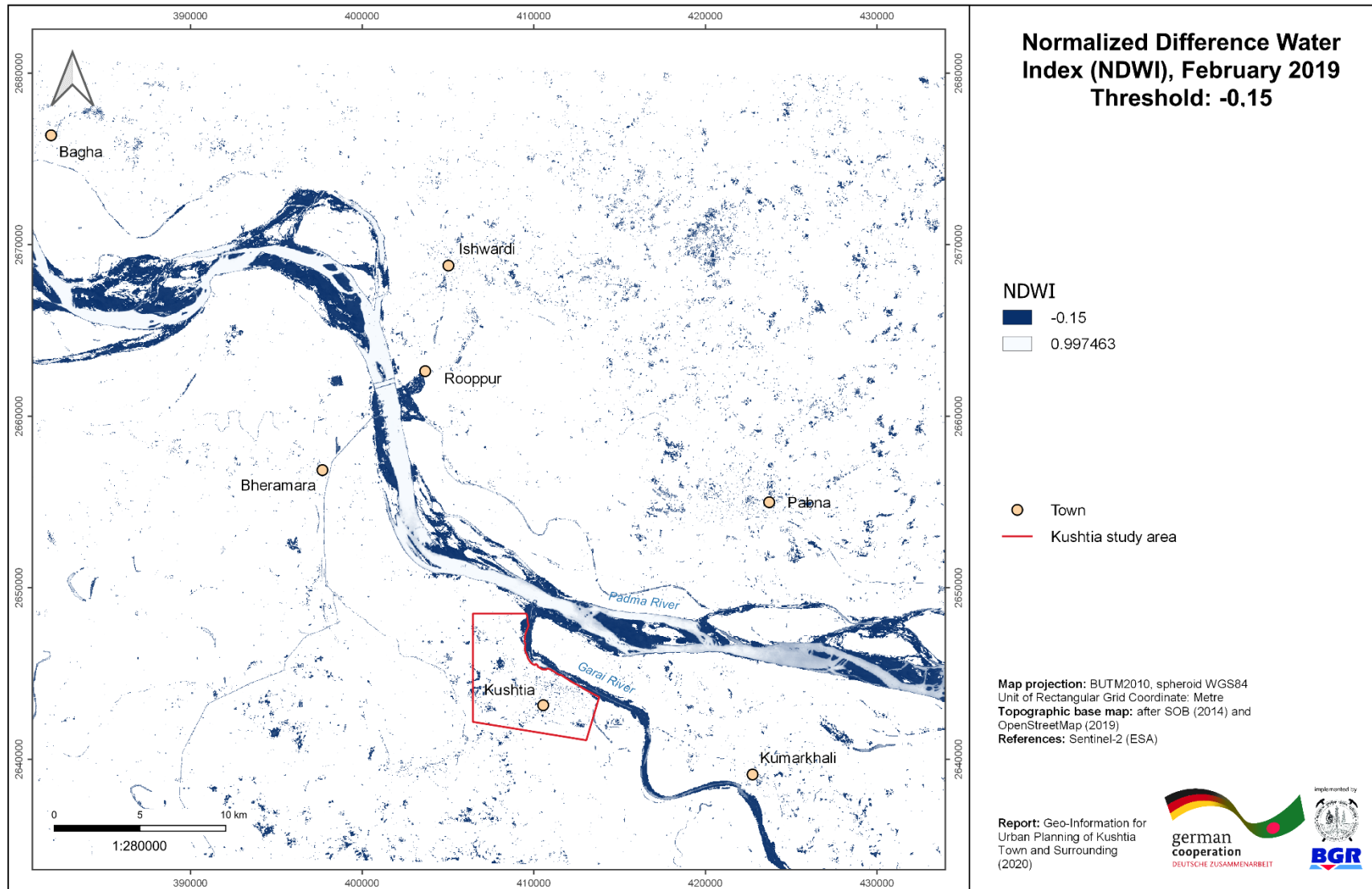


Figure A8: Normalized Difference Water Index (NDWI), based on Sentinel-2 imagery (24.02.2019), Threshold of -0.15.

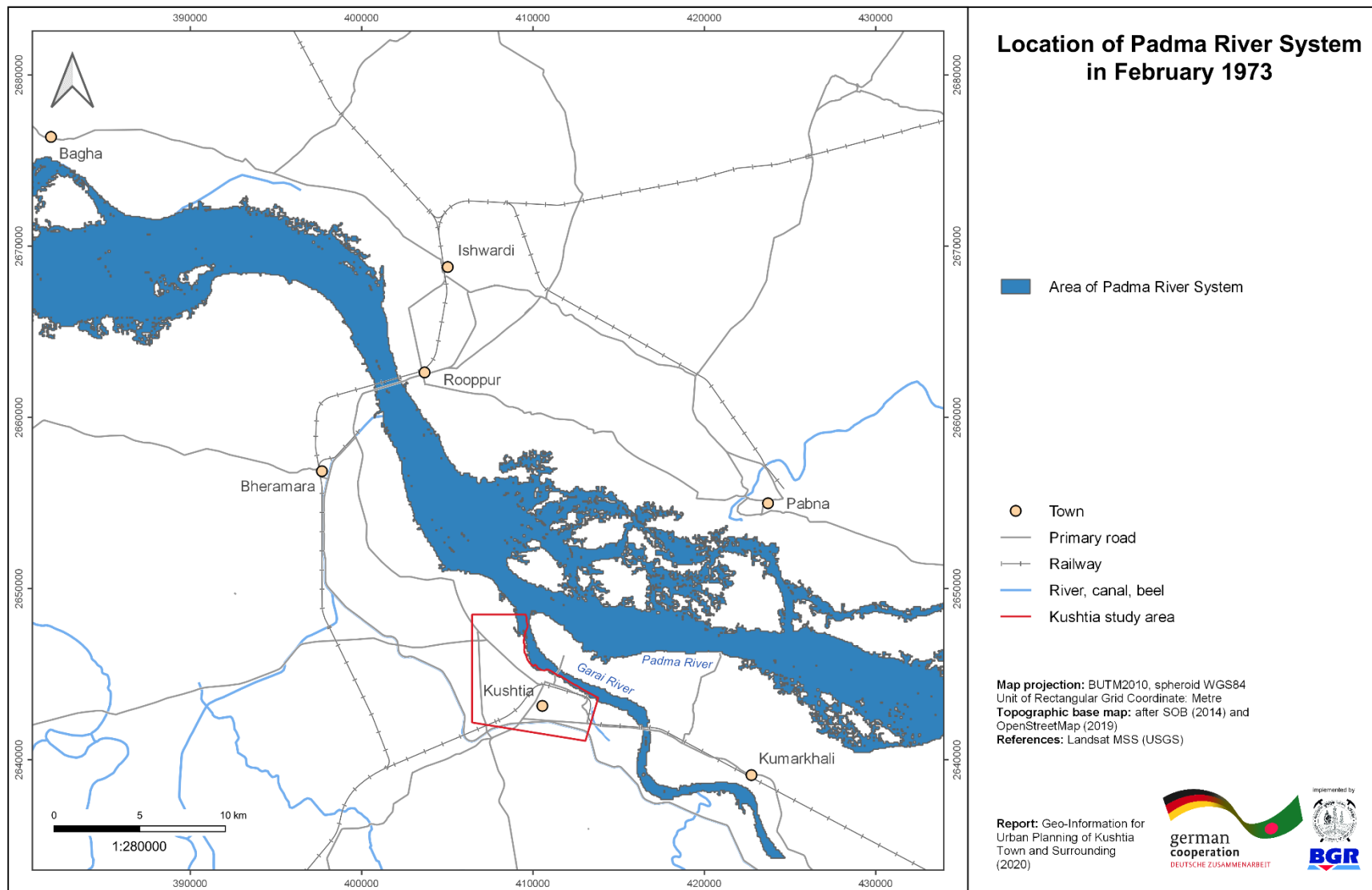


Figure A9: Location of the Padma River System based on NDWI from 1973.

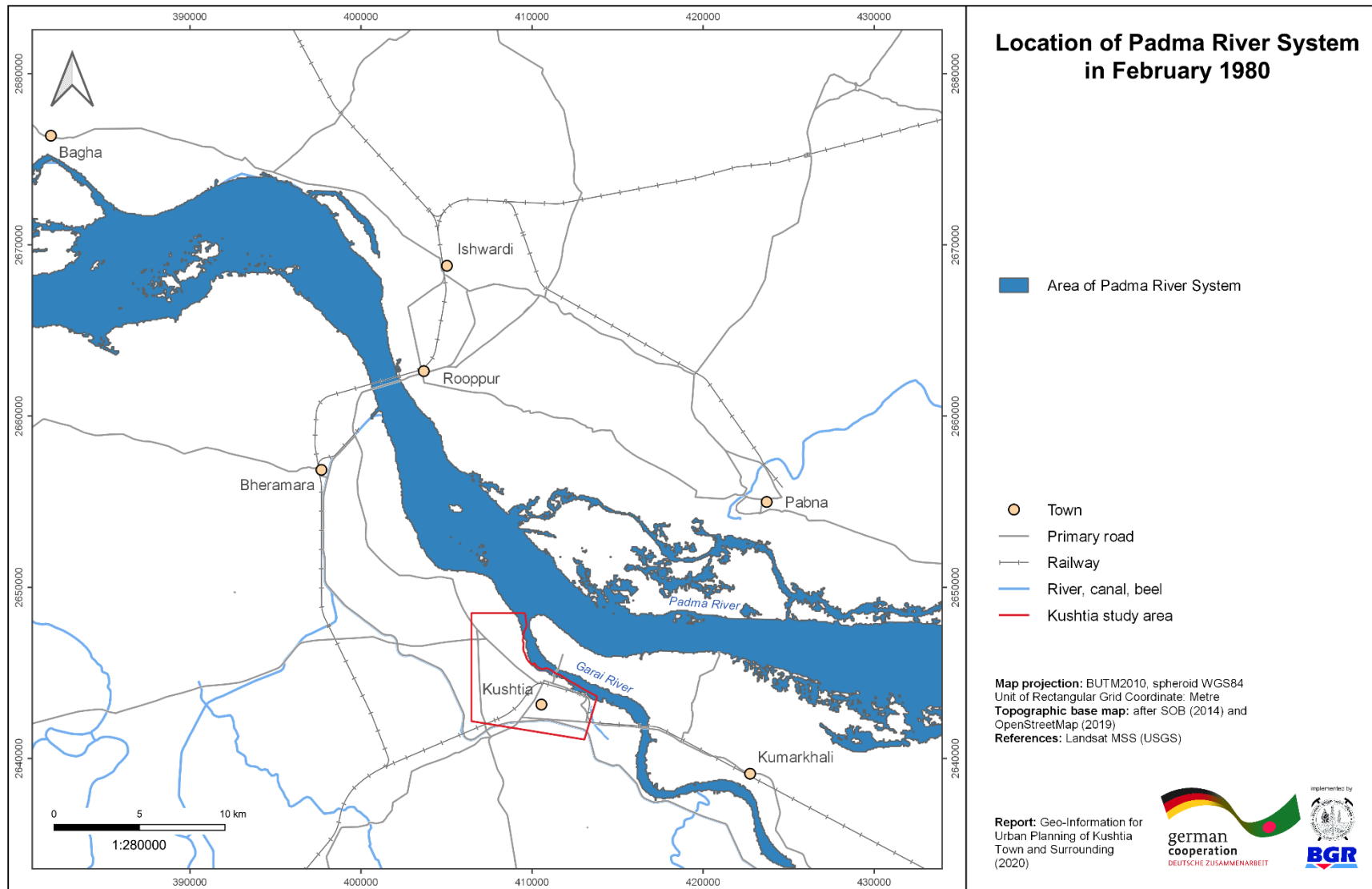


Figure A10: Location of the Padma River System based on NDWI from 1980.

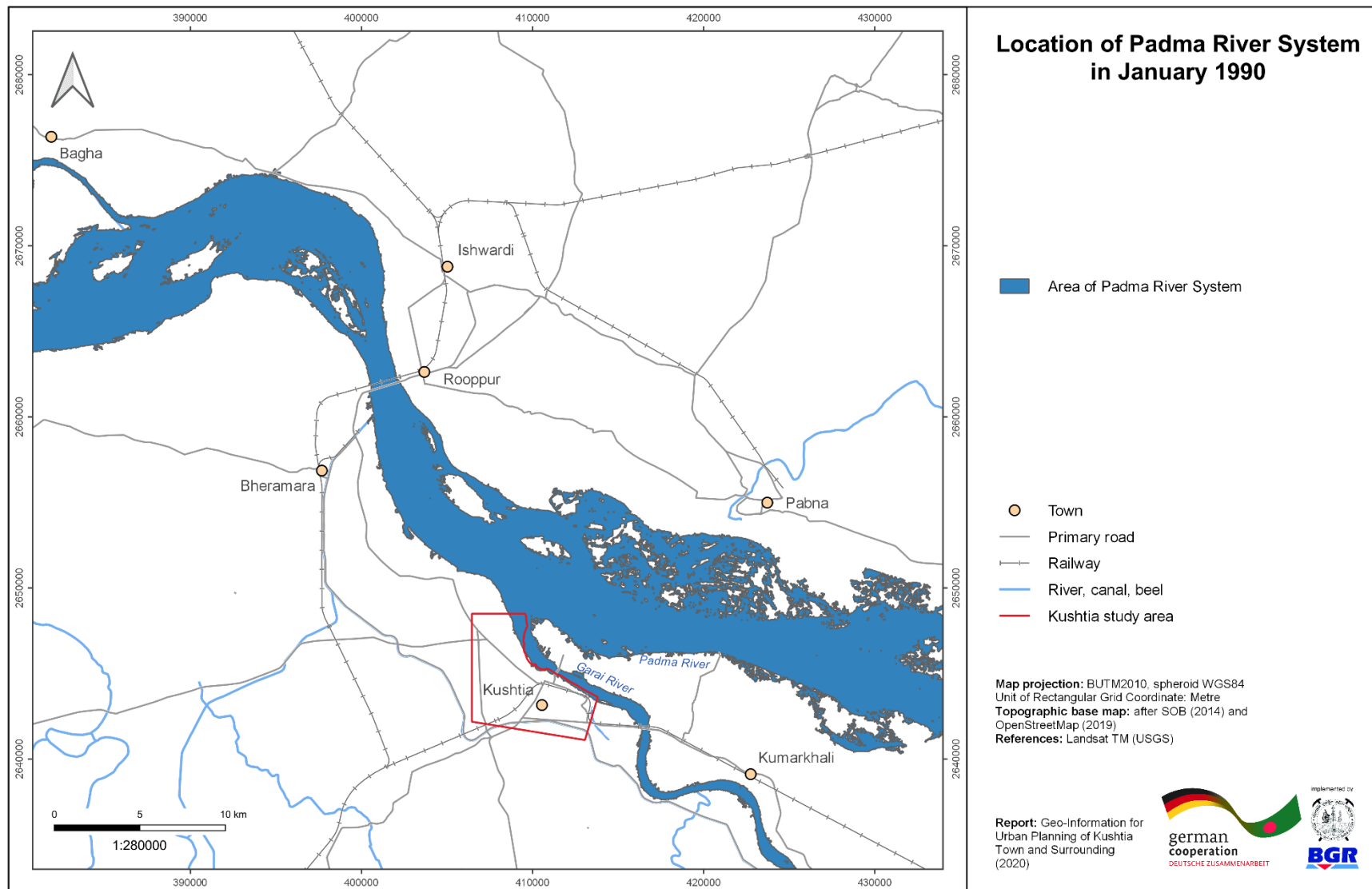


Figure A11: Location of the Padma River System based on NDWI from 1990.

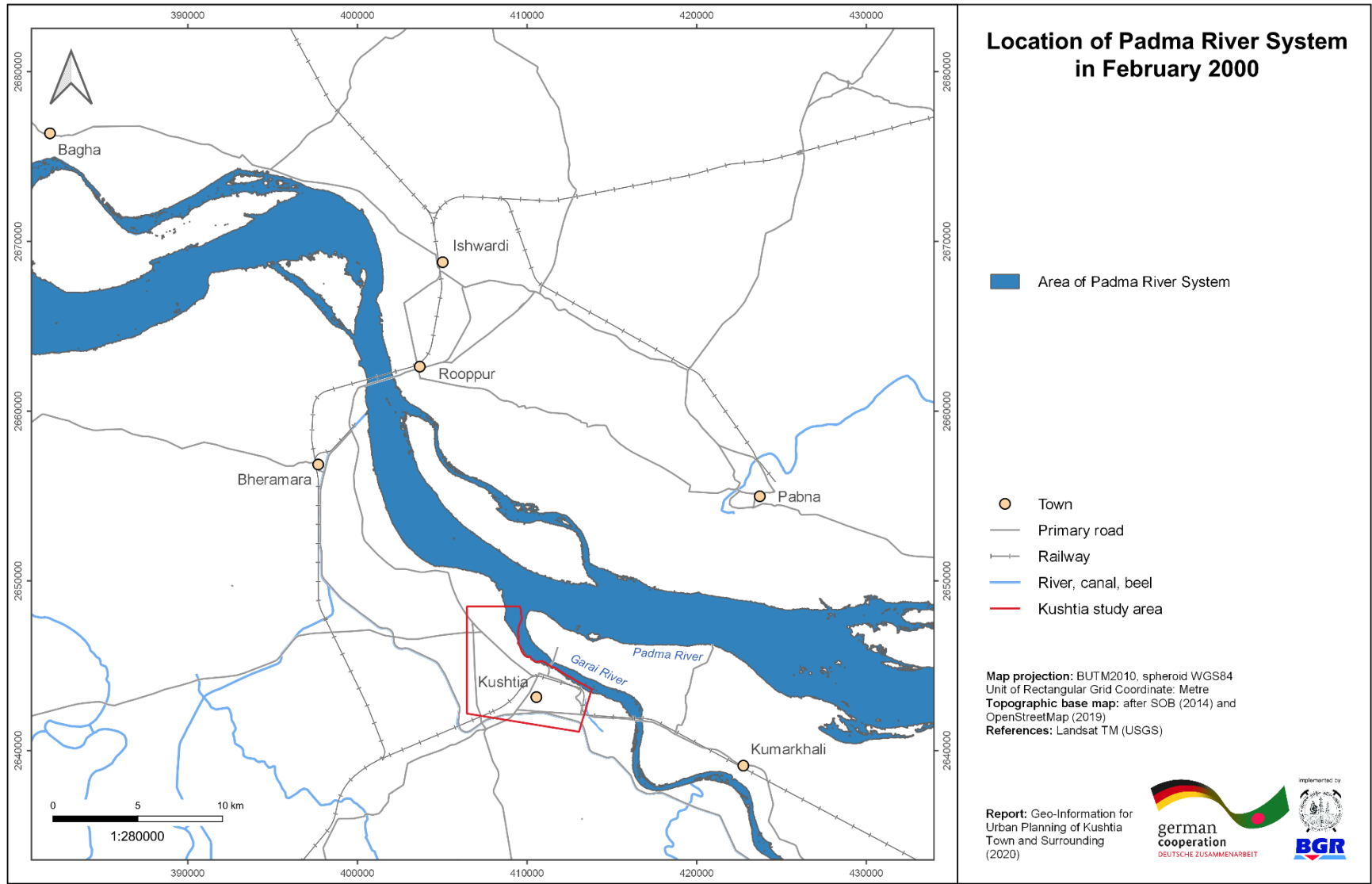


Figure A12: Location of the Padma River System based on NDWI from 2000.

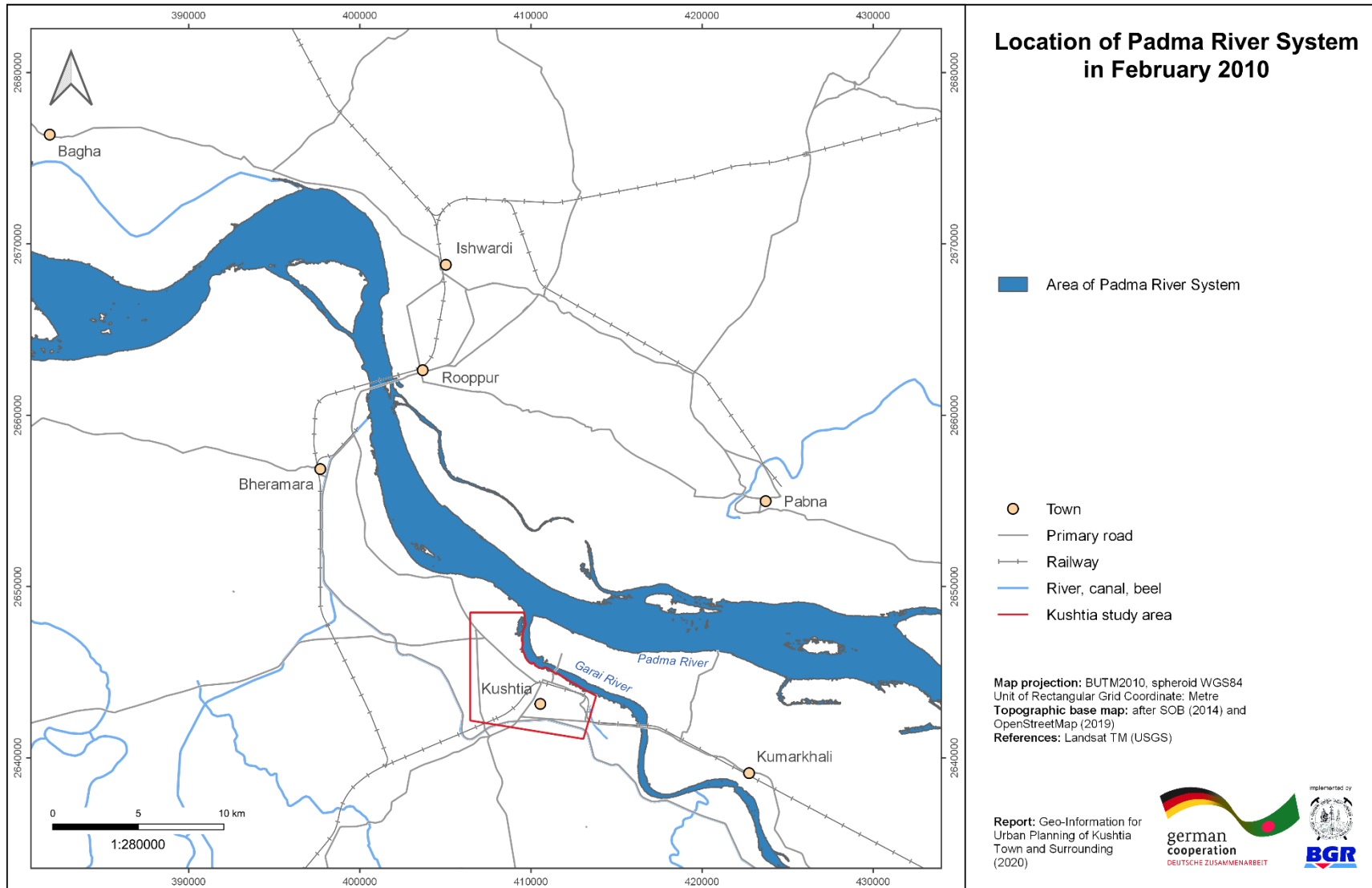


Figure A13: Location of the Padma River System based on NDWI from 2010.

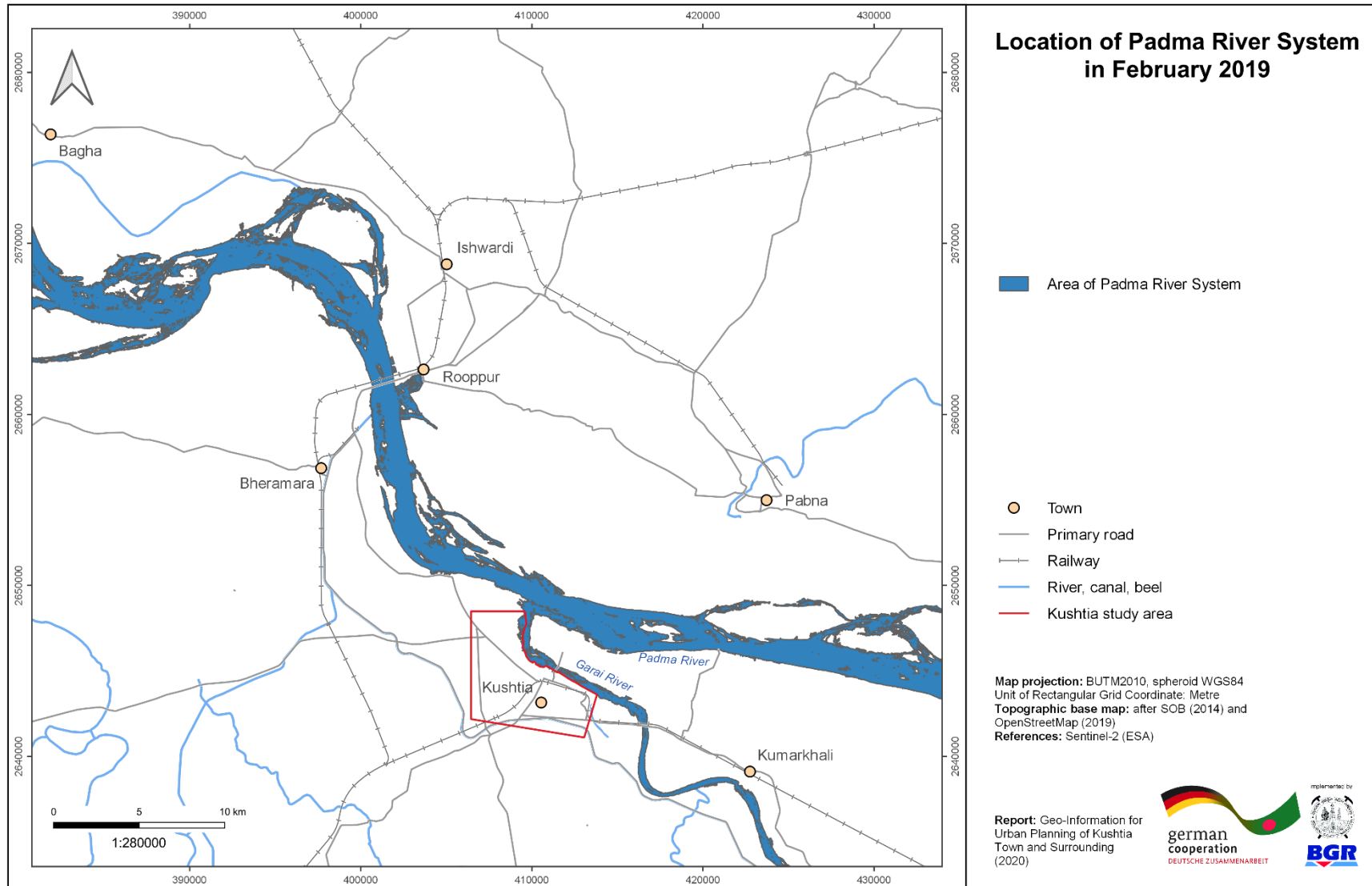


Figure A14: Location of the Padma River System based on NDWI from 2019.

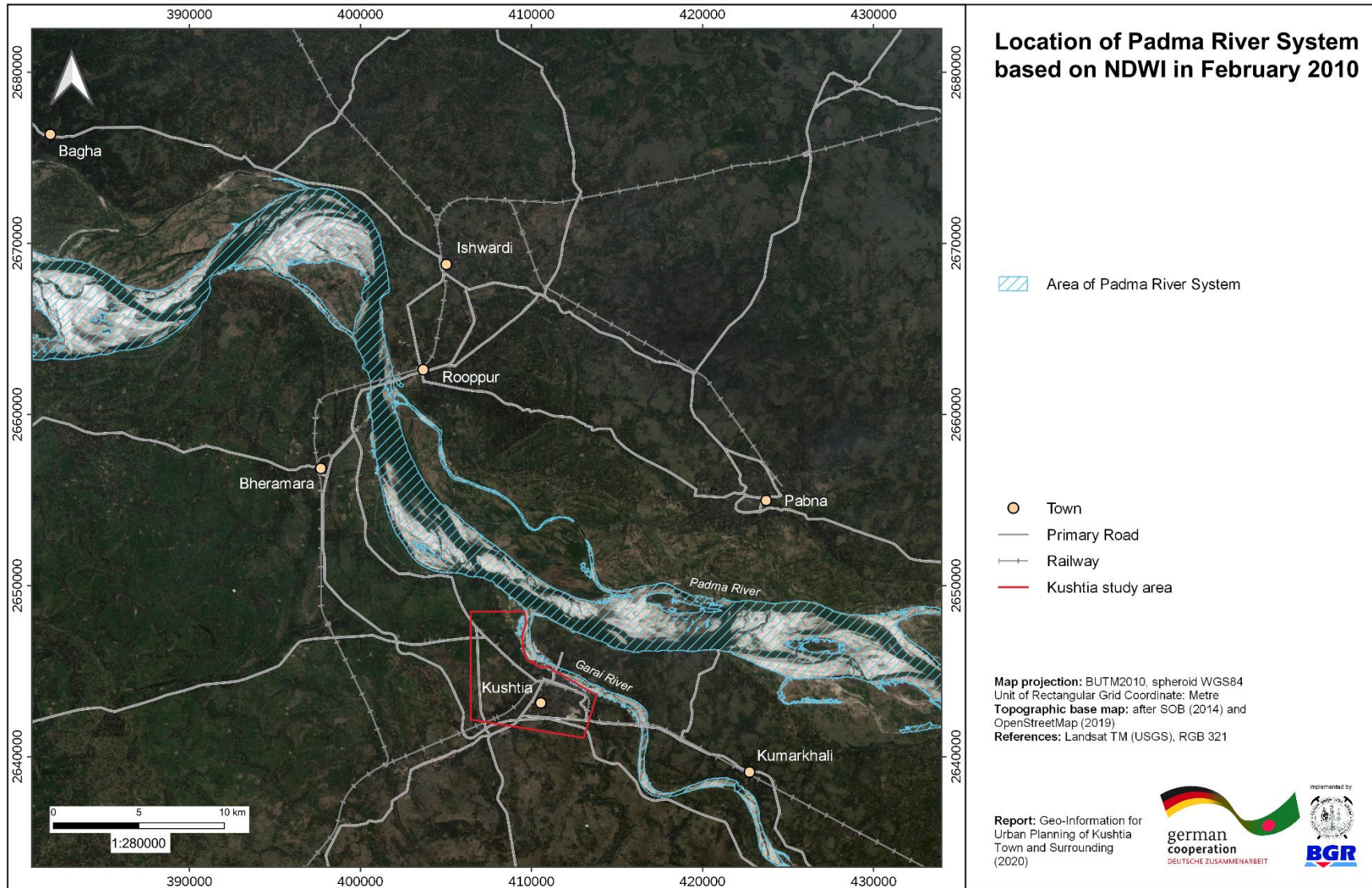


Figure A15: Location of the Padma River System based on NDWI from 2010.

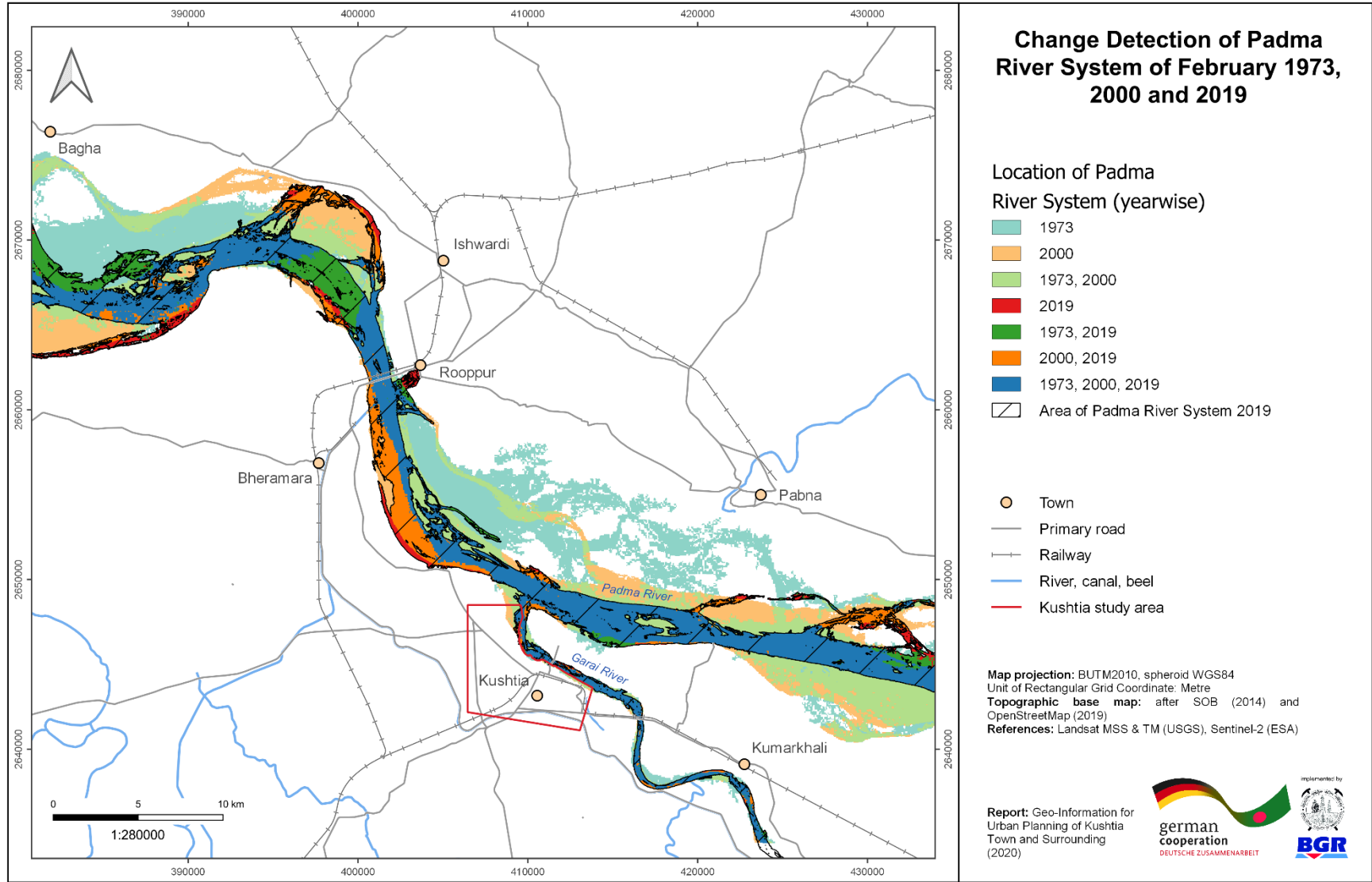


Figure A16: Change Detection of Padma River System of February 1973, 2000 and 2019.

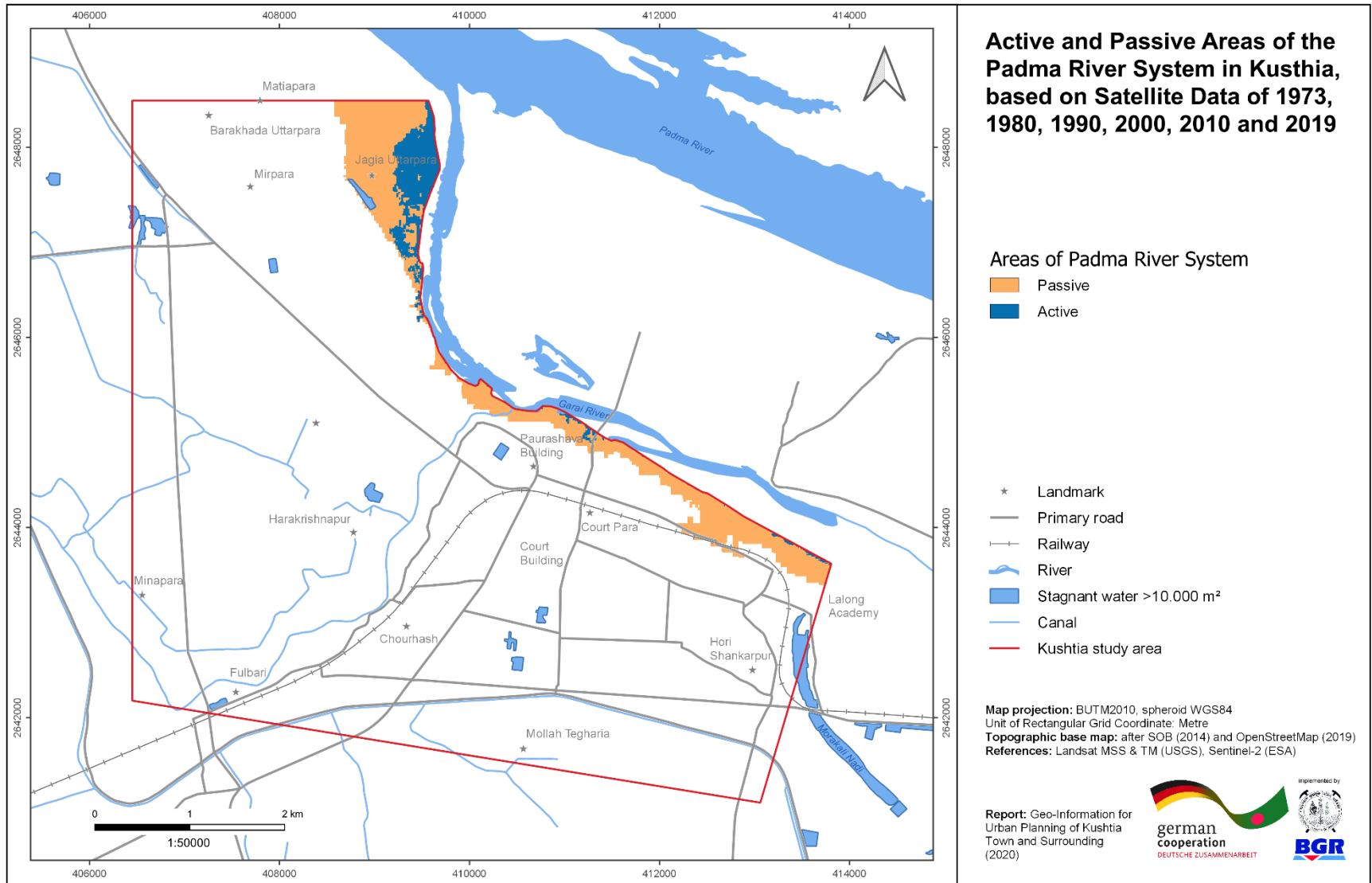


Figure A17: Active and Passive Areas of the Padma River System in Kushtia, based on Satellite Data of 1973, 1980, 1990, 2000, 2010 and 2019.

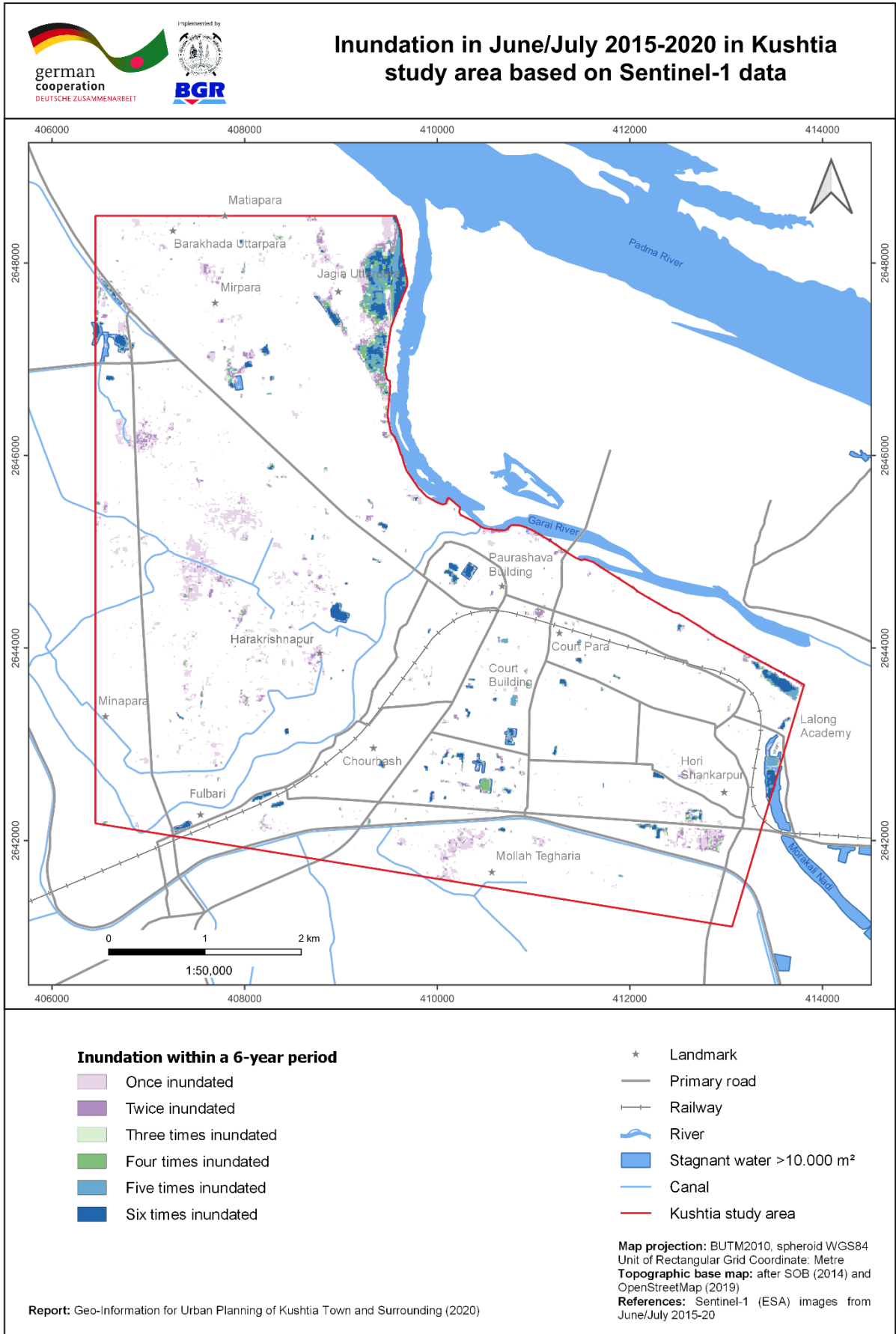


Figure A18: Inundation in June/July 2015-2020 in Kushita study area.

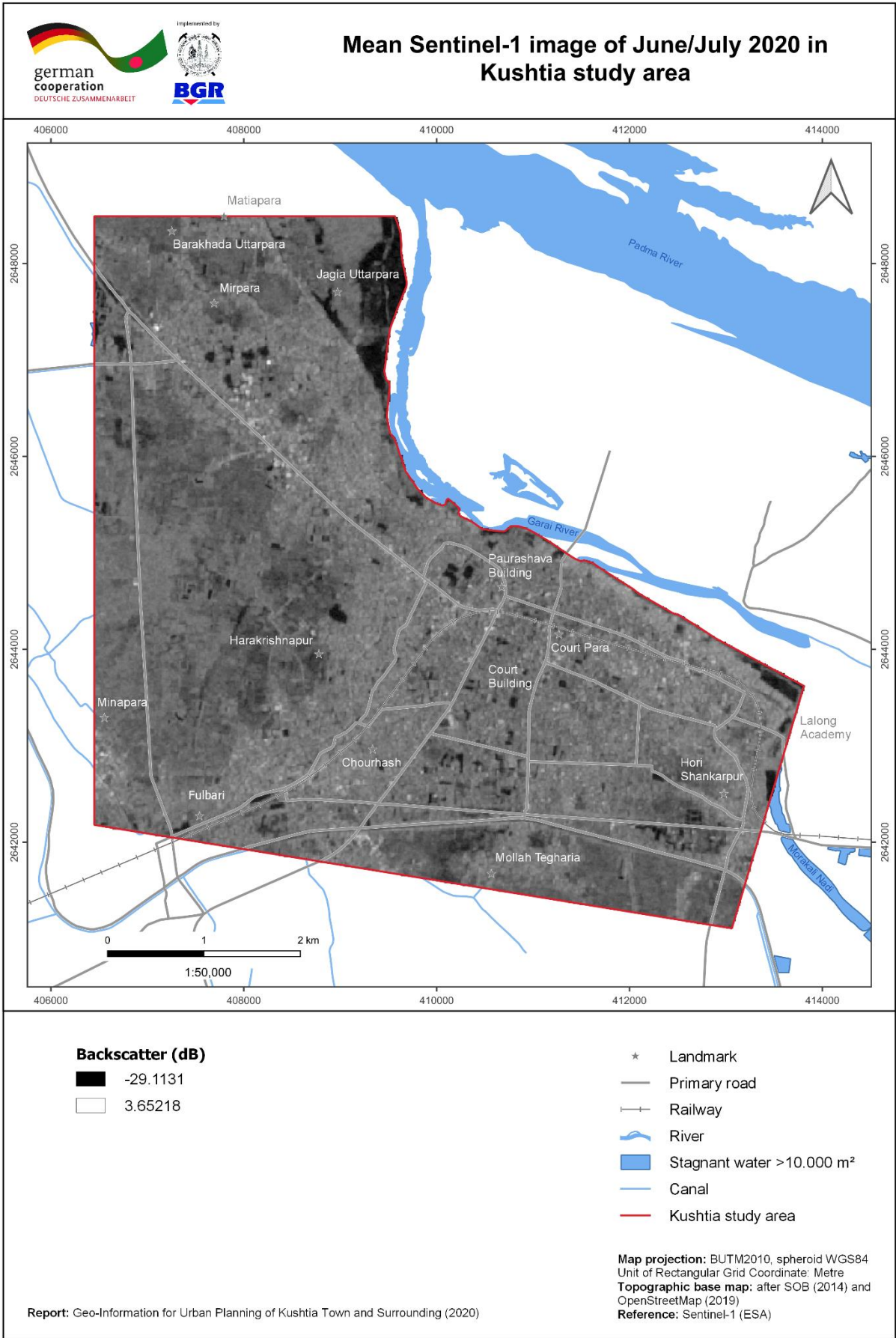



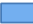


Figure A19: Mean Sentinel-1 image of June/July 2020 in Kushtia study area.

Inundation in June/July 2020 in Kushtia study area based on Sentinel-1 data



Inundation in June/July 2020

 Inundated area

- * Landmark
- Primary road
- +— Railway
-  River
-  Stagnant water >10.000 m²
-  Canal
-  Kushtia study area

Map projection: BUTM2010, spheroid WGS84
 Unit of Rectangular Grid Coordinate: Metre
Topographic base map: after SOB (2014) and OpenStreetMap (2019)
References: Sentinel-1 (ESA) images from June/July 2015-20

Report: Geo-Information for Urban Planning of Kushtia Town and Surrounding (2020)

Figure A20: Inundation in June/July 2020 in Kushita study area.

Annexure B: Google Earth Engine Code

```
1 // Select Area of Interest (KSpa = uploaded SHP of Kushtia study area)
2 KSpa = KSpa.geometry();
3 // Center the map with focus on the study area
4 Map.centerObject(KSpa);
5
6
7 // 2015
8 // Define start and end date of the study period
9 var start_wet = '2015-06-01';
10 var end_wet = '2015-07-30';
11
12 // Load the Sentinel-1 image collection
13 var S1_wet15 = ee.ImageCollection('COPERNICUS/S1_GRD')
14 // Filter: Return only Vertical-Horizontal (VH) polarization images
15 .filter(ee.Filter.listContains('transmitterReceiverPolarisation', 'VH'))
16 // Filter: Return only images with the main acquisition mode IW
17 .filter(ee.Filter.eq('instrumentMode', 'IW'))
18 // Filter: Return only descending orbit images
19 .filter(ee.Filter.eq('orbitProperties_pass', 'DESCENDING'))
20 // Filter: Return only images with a 10 m resolution
21 .filterMetadata('resolution_meters','equals',10)
22 // Filter: Return only images within the study period
23 .filterDate(start_wet, end_wet)
24 // Filter: Return only images within the study area
25 .filterBounds(KSpa)
26 // Calculate the mean of all remaining images
27 .reduce(ee.Reducer.mean())
28 // Clip the mean-image to the study area
29 .clip(KSpa);
30 // Print the image information to the console
31 print(S1_wet15)
32
33
34 // 2016
35 var start_wet = '2016-06-01';
36 var end_wet = '2016-07-30';
37
38 var S1_wet16 = ee.ImageCollection('COPERNICUS/S1_GRD')
```

```

39 .filter(ee.Filter.listContains('transmitterReceiverPolarisation', 'VH'))
40 .filter(ee.Filter.eq('instrumentMode', 'IW'))
41 .filter(ee.Filter.eq('orbitProperties_pass', 'DESCENDING'))
42 .filterMetadata('resolution_meters','equals',10)
43 .filterDate(start_wet, end_wet)
44 .filterBounds(KSpa)
45 .reduce(ee.Reducer.mean())
46 .clip(KSpa);
47 print(S1_wet16)
48
49 // 2017
50 var start_wet = '2017-06-01';
51 var end_wet = '2017-07-30';
52
53 var S1_wet17 = ee.ImageCollection('COPERNICUS/S1_GRD')
54 .filter(ee.Filter.listContains('transmitterReceiverPolarisation', 'VH'))
55 .filter(ee.Filter.eq('instrumentMode', 'IW'))
56 .filter(ee.Filter.eq('orbitProperties_pass', 'DESCENDING'))
57 .filterMetadata('resolution_meters','equals',10)
58 .filterDate(start_wet, end_wet)
59 .filterBounds(KSpa)
60 .reduce(ee.Reducer.mean())
61 .clip(KSpa);
62 print(S1_wet17)
63
64 //2018
65 var start_wet = '2018-06-01';
66 var end_wet = '2018-07-30';
67
68 var S1_wet18 = ee.ImageCollection('COPERNICUS/S1_GRD')
69 .filter(ee.Filter.listContains('transmitterReceiverPolarisation', 'VH'))
70 .filter(ee.Filter.eq('instrumentMode', 'IW'))
71 .filter(ee.Filter.eq('orbitProperties_pass', 'DESCENDING'))
72 .filterMetadata('resolution_meters','equals',10)
73 .filterDate(start_wet, end_wet)
74 .filterBounds(KSpa)
75 .reduce(ee.Reducer.mean())
76 .clip(KSpa);
77 print(S1_wet18)
78
79 //2019
80 var start_wet = '2019-06-01';

```

```

81 var end_wet = '2019-07-30';
82
83 var S1_wet19 = ee.ImageCollection('COPERNICUS/S1_GRD')
84 .filter(ee.Filter.listContains('transmitterReceiverPolarisation', 'VH'))
85 .filter(ee.Filter.eq('instrumentMode', 'IW'))
86 .filter(ee.Filter.eq('orbitProperties_pass', 'DESCENDING'))
87 .filterMetadata('resolution_meters', 'equals', 10)
88 .filterDate(start_wet, end_wet)
89 .filterBounds(KSpa)
90 .reduce(ee.Reducer.mean())
91 .clip(KSpa);
92 print(S1_wet19)
93
94 //2020
95 var start_wet = '2020-06-01';
96 var end_wet = '2020-07-30';
97
98 var S1_wet20 = ee.ImageCollection('COPERNICUS/S1_GRD')
99 .filter(ee.Filter.listContains('transmitterReceiverPolarisation', 'VH'))
100 .filter(ee.Filter.eq('instrumentMode', 'IW'))
101 .filter(ee.Filter.eq('orbitProperties_pass', 'DESCENDING'))
102 .filterMetadata('resolution_meters', 'equals', 10)
103 .filterDate(start_wet, end_wet)
104 .filterBounds(KSpa)
105 .reduce(ee.Reducer.mean())
106 .clip(KSpa);
107 print(S1_wet20)
108
109 // Set threshold to distinguish between water and non-water
110 var threshold = -21
111
112 // Filter every image collection to the defined threshold
113 var S1_wet_threshold15 = S1_wet15.select('VH_mean').lt(threshold);
114 var S1_wet_threshold16 = S1_wet16.select('VH_mean').lt(threshold);
115 var S1_wet_threshold17 = S1_wet17.select('VH_mean').lt(threshold);
116 var S1_wet_threshold18 = S1_wet18.select('VH_mean').lt(threshold);
117 var S1_wet_threshold19 = S1_wet19.select('VH_mean').lt(threshold);
118 var S1_wet_threshold20 = S1_wet20.select('VH_mean').lt(threshold);
119
120 // Combining all images to get one image with six classes

```

```
121 var final_img =
122 S1_wet_threshold15.add(S1_wet_threshold16).add(S1_wet_threshold17).add(S1_w
123 et_threshold18).add(S1_wet_threshold19).add(S1_wet_threshold20);
124
125 // Visualize the final result
126 Map.addLayer(final.updateMask(final_img), {palette: "0000FF"}, 'Water
127 extent', 1);
128
129 // Export the image to the Drive
130 Export.image.toDrive({
131 // Definition of the image
132   image: final_img,
133 // Description
134   description: 'KS_Inundation_Map',
135 // Resolution in meter
136   scale: 20,
137 // Study area
138   region: KSpa,
139 // Format of the raster
140   fileFormat: 'GeoTIFF'
141 });
```

Annexure C: Data

Optical satellite images

Landsat naming convention

Image name (Level-1): LXSS_LLLL_PPPRRR_YYYYMMDD_yyyymmdd_CC_TX

Image name (Level-2): LXSSPPRRRRYYYYMMDDCCTX

Group	Meaning		
LXSS	L: Landsat	X: Sensor "M" (MSS), "T" (TM)	SS: Satellite "01" (Landsat 1), "03" (Landsat 3), "05" (Landsat 5)
LLLL	Processing correction level: "L1TP", "L1GT", "L1GS"		
PPRRR	PPP: WRS path	RRR: WRS row	
YYYYMMDD	Acquisition year, month, day		
yyymmdd	Processing year, month, day		
CC	Collection number: "01", "02", ...		
TX	Collection category: "RT" (Real-Time), "T1" (Tier 1), "T2" (Tier 2)		

Source: usgs.gov/faqs/how-can-i-tell-difference-between-landsat-collections-data-and-landsat-data-i-have-downloaded

(Accessed on 20-07-2020).

Data (Landsat MSS, Level-1)

Year	Image name	Product
1973	LM01_L1TP_148043_19730221_20180427_01_T2	River Shifting Change Detection Analysis
1980	LM03_L1TP_148043_19800221_20180416_01_T2	River Shifting Change Detection Analysis

Data (Landsat TM, Level-2)

Year	Image name	Product
1990	LT051380431990013001T1	River Shifting Change Detection Analysis
2000	LT051380432000021101T1	River Shifting Change Detection Analysis
2010	LT051380432010020601T1	River Shifting Change Detection Analysis

Sentinel-2 naming convention

Image name: MMM_MSIXXX_YYYYMMDDHHMMSS_Nxxyy_ROOO_Txxxxx_<Product Discriminator>

Group	Meaning
MMM	Mission ID: "S2A", "S2B"
MSIXXX	Product level: "Level-1C", "Level-2A"
YYYYMMDDTHHMMSS	Sensing start time, date and time separated by character "T"
Nxxyy	PDGS processing baseline number
ROOO	Relative orbit number
Txxxxx	Tile number

Source: sentinel.esa.int/web/sentinel/user-guides/sentinel-2-msi/naming-convention (Accessed on 20-07-2020).

Data

Year	Image name	Product
2019	S2A_MSIL1C_20190224T043751_N0207_R033_T45QYG_20190224T081535	River Shifting Change Detection Analysis
	S2A_MSIL1C_20190224T043751_N0207_R033_T45QXG_20190224T081535	River Shifting Change Detection Analysis
	S2A_MSIL2A_20190922T043701_N0213_R033_T45QYG_20190922T084016	Land-Use Classification

RADAR satellite images

Sentinel-1 naming convention

Image name: MMM_BB_TTTR_LFPP_YYYYMMDDTHHMMSS_YYYYMMDDTHHMMSS_OOOOOO_DDDDDD_CCCC

Group	Meaning		
MMM	Mission Identifier: "S1A", "S1B"		
BB	Mode/Beam: "S1/S2/S3/S4/S5/S6", "IW/EW/WV"		
TTTR	TTT: Product Type "RAW", "SLC", "GRD", "OCN"		R: Resolution Class "F" (Full), "H" (High), "M" (Medium)
LFPP	L: Processing Level "0", "1", "2"	F: Product Class "S" (Standard), "A" (Annotation)	PP: Polarization "SH" (single HH) "SV" (single VV) "DH" (dual HH+HV)

			"DV" (dual VV+VH)
YYYYMMDDTHHMMSS	Product start time, separated by the character "T"		
YYYYMMDDTHHMMSS	Product end time, separated by the character "T"		
OOOOOO	Absolute orbit number at product start time		
DDDDDD	Mission data-take identifier		
CCCC	Product unique identifier		

Source: sentinel.esa.int/web/sentinel/user-guides/sentinel-1-sar/naming-conventions (Accessed on 20-07-2020).

Data

Year	Image Name
2015	S1A_IW_GRDH_1SDV_20150612T235524_20150612T235549_006347_0085AA_C142
	S1A_IW_GRDH_1SDV_20150630T000327_20150630T000352_006595_008CA0_2C75
	S1A_IW_GRDH_1SDV_20150706T235524_20150706T235549_006697_008F55_E0E4
	S1A_IW_GRDH_1SDV_20150724T000327_20150724T000352_006945_009672_27AA
2016	S1A_IW_GRDH_1SDV_20160606T235527_20160606T235552_011597_011B95_1F08
	S1A_IW_GRDH_1SDV_20160630T235528_20160630T235553_011947_0126A4_AB04
	S1A_IW_GRDH_1SDV_20160718T000336_20160718T000401_012195_012EC8_FCF2
	S1A_IW_GRDH_1SDV_20160724T235529_20160724T235554_012297_013213_0790
2017	S1A_IW_GRDH_1SDV_20170601T235528_20170601T235553_016847_01C031_F847
	S1A_IW_GRDH_1SDV_20170607T000336_20170607T000401_016920_01C27F_10E4
	S1A_IW_GRDH_1SDV_20170607T000401_20170607T000426_016920_01C27F_83A0

	S1A_IW_GRDH_1SDV_20170619T000337_20170619T000402_017095_01C7E1_9AF9
	S1A_IW_GRDH_1SDV_20170619T000402_20170619T000427_017095_01C7E1_9B0D
	S1A_IW_GRDH_1SDV_20170701T000337_20170701T000402_017270_01CD28_970D
	S1A_IW_GRDH_1SDV_20170701T000402_20170701T000427_017270_01CD28_C453
	S1A_IW_GRDH_1SDV_20170725T000339_20170725T000404_017620_01D7C9_F531
	S1A_IW_GRDH_1SDV_20170725T000404_20170725T000429_017620_01D7C9_DCFD
2018	S1A_IW_GRDH_1SDV_20180608T235535_20180608T235600_022272_026907_035D
	S1A_IW_GRDH_1SDV_20180614T000343_20180614T000408_022345_026B4E_8A5D
	S1A_IW_GRDH_1SDV_20180614T000408_20180614T000433_022345_026B4E_51E8
	S1A_IW_GRDH_1SDV_20180626T000343_20180626T000408_022520_027072_2425
	S1A_IW_GRDH_1SDV_20180626T000408_20180626T000433_022520_027072_6AE7
	S1A_IW_GRDH_1SDV_20180708T000344_20180708T000409_022695_02758B_A657
	S1A_IW_GRDH_1SDV_20180708T000409_20180708T000434_022695_02758B_A5FE
	S1A_IW_GRDH_1SDV_20180714T235537_20180714T235602_022797_0278AA_2752
	S1A_IW_GRDH_1SDV_20180720T000345_20180720T000410_022870_027AE8_BE68
	S1A_IW_GRDH_1SDV_20180720T000410_20180720T000435_022870_027AE8_BC82
	S1A_IW_GRDH_1SDV_20180726T235538_20180726T235603_022972_027E33_C265
2019	S1A_IW_GRDH_1SDV_20190603T235541_20190603T235606_027522_031B0C_A98E
	S1A_IW_GRDH_1SDV_20190615T235541_20190615T235606_027697_032055_BC0D
	S1A_IW_GRDH_1SDV_20190627T235542_20190627T235607_027872_03258C_31FD
	S1A_IW_GRDH_1SDV_20190709T235543_20190709T235608_028047_032AE1_1F4E

	S1A_IW_GRDH_1SDV_20190721T235544_20190721T235609_028222_033027_264C
	S1A_IW_GRDH_1SDV_20190727T000351_20190727T000416_028295_033259_7B24
	S1A_IW_GRDH_1SDV_20190727T000416_20190727T000441_028295_033259_7B89
2020	S1A_IW_GRDH_1SDV_20200603T000355_20200603T000420_032845_03CDEB_5865
	S1A_IW_GRDH_1SDV_20200603T000420_20200603T000445_032845_03CDEB_D620
	S1A_IW_GRDH_1SDV_20200609T235548_20200609T235613_032947_03D0F8_ABCE
	S1A_IW_GRDH_1SDV_20200615T000355_20200615T000420_033020_03D320_436E
	S1A_IW_GRDH_1SDV_20200615T000420_20200615T000445_033020_03D320_F045
	S1A_IW_GRDH_1SDV_20200621T235549_20200621T235614_033122_03D646_CC28
	S1A_IW_GRDH_1SDV_20200627T000356_20200627T000421_033195_03D870_5BC2
	S1A_IW_GRDH_1SDV_20200627T000421_20200627T000446_033195_03D870_EF60
	S1A_IW_GRDH_1SDV_20200703T235549_20200703T235614_033297_03DB97_B775
	S1A_IW_GRDH_1SDV_20200709T000357_20200709T000422_033370_03DDC1_FABB
	S1A_IW_GRDH_1SDV_20200709T000422_20200709T000447_033370_03DDC1_BB58
	S1A_IW_GRDH_1SDV_20200715T235550_20200715T235615_033472_03E0EC_41A1
	S1A_IW_GRDH_1SDV_20200721T000358_20200721T000423_033545_03E31B_1D39
	S1A_IW_GRDH_1SDV_20200721T000423_20200721T000448_033545_03E31B_29E3
	S1A_IW_GRDH_1SDV_20200727T235551_20200727T235616_033647_03E64C_0433
	S1B_IW_GRDH_1SDV_20200721T235523_20200721T235548_022576_02AD94_45A2